nature chemical biology

Article

https://doi.org/10.1038/s41589-024-01702-5

Shifting redox reaction equilibria on demand using an orthogonal redox cofactor

Received: 20 October 2023

Accepted: 16 July 2024

Published online: 13 August 2024

Check for updates

Derek Aspacio[1,9], Yulai Zhang[1,9], Youtian Cui[2,9], Emma Luu[2], Edward King[3], William B. Black[1], Sean Perea[1], Qiang Zhu[1,3,4,5], Yongxian Wu[1,3,4,5], Ray Luo[1,3,4,5], Justin B. Siegel[2,6,7] & Han Li[1,5,8]

Nature's two redox cofactors, nicotinamide adenine dinucleotide (NAD^+) and nicotinamide adenine dinucleotide phosphate ($NADP^+$), are held at different reduction potentials, driving catabolism and anabolism in opposite directions. In biomanufacturing, there is a need to flexibly control redox reaction direction decoupled from catabolism and anabolism. We established nicotinamide mononucleotide (NMN^+) as a noncanonical cofactor orthogonal to $NAD(P)^+$. Here we present the development of Nox Ortho, a reduced NMN^+ (NMNH)-specific oxidase, that completes the toolkit to modulate NMNH:NMN^+ ratio together with an NMN^+-specific glucose dehydrogenase (GDH Ortho). The design principle discovered from Nox Ortho engineering and modeling is facilely translated onto six different enzymes to create NMN(H)-orthogonal biocatalysts with a consistent ~10^3–10^6-fold cofactor specificity switch from $NAD(P)^+$ to NMN^+. We assemble these enzymes to produce stereo-pure 2,3-butanediol in cell-free systems and in *Escherichia coli*, enabled by NMN(H)'s distinct redox ratio firmly set by its designated driving forces, decoupled from both NAD(H) and NADP(H).

Biomanufacturing of renewable chemicals by engineered microbes[1,2] or synthetic biochemistry[3] has the potential to supplant many petroleum-derived chemical industries[4]. However, many engineered biosynthetic pathways fail to proceed past laboratory scale because of insufficient titer, productivity or yield[5]. One prevalent obstacle to these goals is redox imbalance. The chassis organisms that provide high-energy cofactors[6] also contain numerous competing pathways, which drain these critical resources. However, most of these competing pathways must remain intact because life-essential biomass precursors are produced. The exogeneous addition of high-energy cofactors can potentially mitigate the issue; however, the cost and stability of natural cofactors pose concerns for large-scale applications[7–10]. Thus, redox-dependent industrial bioprocesses must achieve a delicate balance among the cell's redox homeostasis, a source of life-essential metabolites and the redox balance of a complete biotransformation. We and others have proposed that orthogonal metabolic systems could solve this limitation through specific delivery of resources[11–15].

Nature uses two different redox cofactors, nicotinamide adenine dinucleotide (NAD^+) and nicotinamide adenine dinucleotide phosphate ($NADP^+$), to provide separate driving forces ensuring that catabolism and anabolism, respectively, proceed in opposite directions by maintaining a low reduced NAD^+ (NADH):NAD^+ ratio and a high reduced $NADP^+$ (NADPH):$NADP^+$ ratio[16–18]. This principle has been recapitulated in cell-free systems[16,19–21].

Therefore, in whole-cell biomanufacturing, the dependence on NAD(H) and NADP(H) permanently ties the reaction direction of a desired redox reaction to either catabolism or anabolism. This does not allow flexible control of reaction equilibrium. In cell-free

[1]Department of Chemical and Biomolecular Engineering, University of California, Irvine, Irvine, CA, USA. [2]Genome Center, University of California, Davis, Davis, CA, USA. [3]Department of Molecular Biology and Biochemistry, University of California, Irvine, Irvine, CA, USA. [4]Department of Material Science and Engineering, University of California, Irvine, Irvine, CA, USA. [5]Department of Biomedical Engineering, University of California, Irvine, Irvine, CA, USA. [6]Department of Chemistry, University of California, Davis, Davis, CA, USA. [7]Department of Biochemistry and Molecular Medicine, University of California, Davis, Davis, CA, USA. [8]Department of Biological Chemistry, University of California, Irvine, Irvine, CA, USA. [9]These authors contributed equally: Derek Aspacio, Yulai Zhang, Youtian Cui. e-mail: han.li@uci.edu

biomanufacturing, NADP(H) is avoided because of its formidable cost and low stability[8,9]. This leaves NAD(H) as the sole electron carrier, which alone cannot support thermodynamically uphill oxidation and reduction reactions simultaneously without forming a futile cycle[16].

These limitations associated with relying on natural cofactors have motivated the development of noncanonical cofactors[7,12,14,15,22–27]. Previously, we established a noncanonical redox cofactor, nicotinamide mononucleotide (NMN^+), which operates in an orthogonal fashion to $NAD(P)^+$ to precisely channel reducing power in *Escherichia coli* whole cells and crude lysates[12,15,28–30]. NMN^+ is also a lower-cost alternative to $NAD(P)^+$ (refs. 10,31) and we have leveraged it to sustain industrially relevant total turnover numbers in cell-free reactions[12,29].

Here, we develop a reduced NMN^+ (NMNH)-specific oxidase (Nox Ortho) derived from *Lactobacillus lactis* water-forming NADH oxidase (*Ll* Nox) through a high-throughput, growth-based selection[28]. Together with the NMN^+-specific glucose dehydrogenase (GDH Ortho) we previously engineered[12], this work completes the toolkit to modulate the NMNH:NMN^+ ratio. We establish that the NMN(H) cofactor pool can be held at a distinct redox ratio on demand (ranging from 70 to 0.07 for NMNH:NMN^+), which is decoupled from both NAD(H) and NADP(H) redox ratios in vitro and in vivo. By designing (*S*)-specific butanediol (BDO) dehydrogenases (Bdhs) to specifically use NMN(H), we tap into this orthogonal driving force to produce chiral-pure 2,3-BDO with a high degree of completion, without interference by the NAD(P)/H reduction potentials in vitro and in vivo.

More importantly, this work also points out a path to readily broaden the applications of this unwavering redox driving force. The enzyme design principle discovered from directed evolution of Nox Ortho, namely, to restrict the cofactor-binding pocket with hydrogen bonding, is consistently translated onto six Bdh enzymes to create NMN(H)-orthogonal catalysts. On different enzyme scaffolds, this strategy consistently results in a 1.0×10^3–3.0×10^6-fold switch of cofactor specificity from NAD(H) or NADP(H) to NMN(H) relative to wild type (WT). Given the conserved positions of these amino acid substitutions, we envision rapidly extending this design principle to other redox enzymes that catalyze key steps in biomanufacturing where precise equilibrium control is needed.

Results and discussion

Stereo-upgrading as a test bed for orthogonal driving forces

BDO is an important biobased chiral chemical with broad industrial applications such as synthetic rubbers[32,33], fuels[32,33], and pharmaceuticals[33]. BDO exists as three stereoisomers (Fig. 1): (2*S*,3*R*)-*meso*-butanediol (*m*-BDO), (2*S*,3*S*)-butanediol ((*SS*)-BDO), and (2*R*,3*R*)-butanediol ((*RR*)-BDO). The goal of the system we establish here is to convert *m*-BDO to either (*SS*)-BDO or (*RR*)-BDO with high purity, which is a value-added process[34–36].

The challenge in this process is that it requires two contradicting steps to both go to completion. First, an oxidation destroys a specific chiral center to yield acetoin (Ac). Second, a reduction installs a new chiral center (the four proposed designs are shown in Fig. 1a–d and discussed below). If these two reaction steps use the same cofactor, for example, NAD(H), then the NADH:NAD^+ ratio would need to be kept low for step one and high for step two. This is not feasible if both steps occur simultaneously in the same space (Fig. 1e). When NAD(H) is incubated with 5 g l^{-1} *m*-BDO and multiple Bdhs with different stereospecificities (the different enzyme classes are depicted in Fig. 1f) in the absence of cofactor-recycling reactions to drive either step to completion, the result is a nearly equal distribution of *m*-BDO, (*SS*)-BDO and (*RR*)-BDO (Fig. 1g). This is because both oxidation and reduction steps suffer from the low driving force that stems from a suboptimal NADH:NAD^+ ratio and these enzymes operate in a fully reversible fashion. When an oxidation driving force is introduced by coupling to a water-forming NADH oxidase (*Lactobacillus brevis* Nox WT)[37], the NADH:NAD^+ ratio is held low and the reaction only completes the first oxidation step on *m*-BDO, yielding a mixture of (*S*)-Ac and (*R*)-Ac (Fig. 1h). On the other hand, when a reduction driving force is introduced by NAD^+-reducing GDH (*Bacillus subtilis* WT)[12], the NADH:NAD^+ ratio is held high and the reaction does not proceed past step one; *m*-BDO remains untransformed (Fig. 1i).

Broadly, current solutions to this problem are twofold. First, the two steps can be compartmentalized into separate cells with inverse NADH:NAD^+ ratios[34–36]. This approach requires the intermediate to build up to a substantial level and readily diffuse across the cell membrane, which limits the scope of conversion. For example, complex and low-concentration intermediates in natural product biosynthetic pathways may not meet these requirements. In vitro, compartmentalization is also challenging to achieve. Second, NADP(H) can be assigned as the reducing cofactor and NAD(H) can be assigned as the oxidizing cofactor. However, although many natural or engineered enzymes can have a preference between NAD(H) and NADP(H), most are promiscuous to both cofactors to a substantial degree[38] because of the intrinsic high similarity between the two cofactors. Therefore, obtaining a strongly NAD(H)-specific enzyme for every oxidizing step and an NADP(H)-specific one for every reducing step is not always feasible, especially as the number of pathway steps increases. Furthermore, the reduction potential of NAD(H) and NADP(H) can become connected in vivo depending on the cell's metabolic state[39–42] and NADP(H) is too expensive to use at large scale in vitro[8,9,39,43,44].

Our BDO-upgrading model system illustrates that, when limited to a single cofactor, metabolic pathways are unable to complete two contradicting steps no matter whether or how the driving force is applied. When two or more cofactors are used with enzymatic crosstalk among them (for example, NAD(H) and NADP(H)), the outcome resembles the single-cofactor system to some degree, dependent on the rate of crosstalk. This justifies a fundamental design principle in metabolism; orthogonality permits thermodynamically incompatible reactions to occur simultaneously.

In our design, we aimed to use NMN(H) flexibly as either the reducing or the oxidizing cofactor and demonstrate that it can be paired with either NAD(H) or NADP(H) as the opposing cofactor, without crosstalk in the same space. This results in a total of four combinations in cofactor use (Fig. 1a–d). Here, we chose to engineer the enzymes that specifically destroy or install the (*S*)-chiral center to use NMN(H) (Fig. 1f). If NMN(H) is an orthogonal redox driving force that is insulated from both NAD(H) and NAD(P)H, two of the four cofactor combinations will yield pure (*SS*)-BDO (Fig. 1a,c) and the other two will yield pure (*RR*)-BDO (Fig. 1b,d). To demonstrate the versatility of our method compared to the two existing approaches mentioned above, we test both in vitro and in vivo in the same *E. coli* cells without compartmentalization.

Development of an orthogonal NMNH oxidase

For NMN(H) to drive either oxidation or reduction on demand, our design requires two orthogonal and complimentary NMN(H) cycling enzymes. To maintain a high NMNH:NMN^+ ratio, we use our previously engineered GDH Ortho[12]. To maintain a low NMNH:NMN^+ ratio, we sought to engineer an orthogonal NMNH oxidase (Nox Ortho) based on the water-forming NADH oxidase. Water-forming oxidases (Nox) catalyze the reaction of reduced cofactor with oxygen and provide a byproduct-free and high-driving-force reaction to rapidly recycle NAD(P)H to $NAD(P)^+$ in reported bioprocesses[21,44–47]. In recent work, the Nox from *L. pentosus* (*Lp* Nox) was engineered to accept NMNH and other noncanonical cofactors[28]. However, *Lp* Nox still retains activity toward NADH and NADPH. As discussed above, cofactor promiscuity is undesirable because it breaks the insulation between separate driving forces.

Here, we started with a new Nox scaffold from *L. lactis* because of its high affinity for oxygen, broad operational pH and temperature ranges, and robust applications in vitro and in vivo[48–50]. To enable NMNH activity, we migrated a similar rational design from *Lp* Nox to *Ll* Nox (namely, the I159T substitution), which resulted in a ~20-fold

https://doi.org/10.1038/s41589-024-01702-5

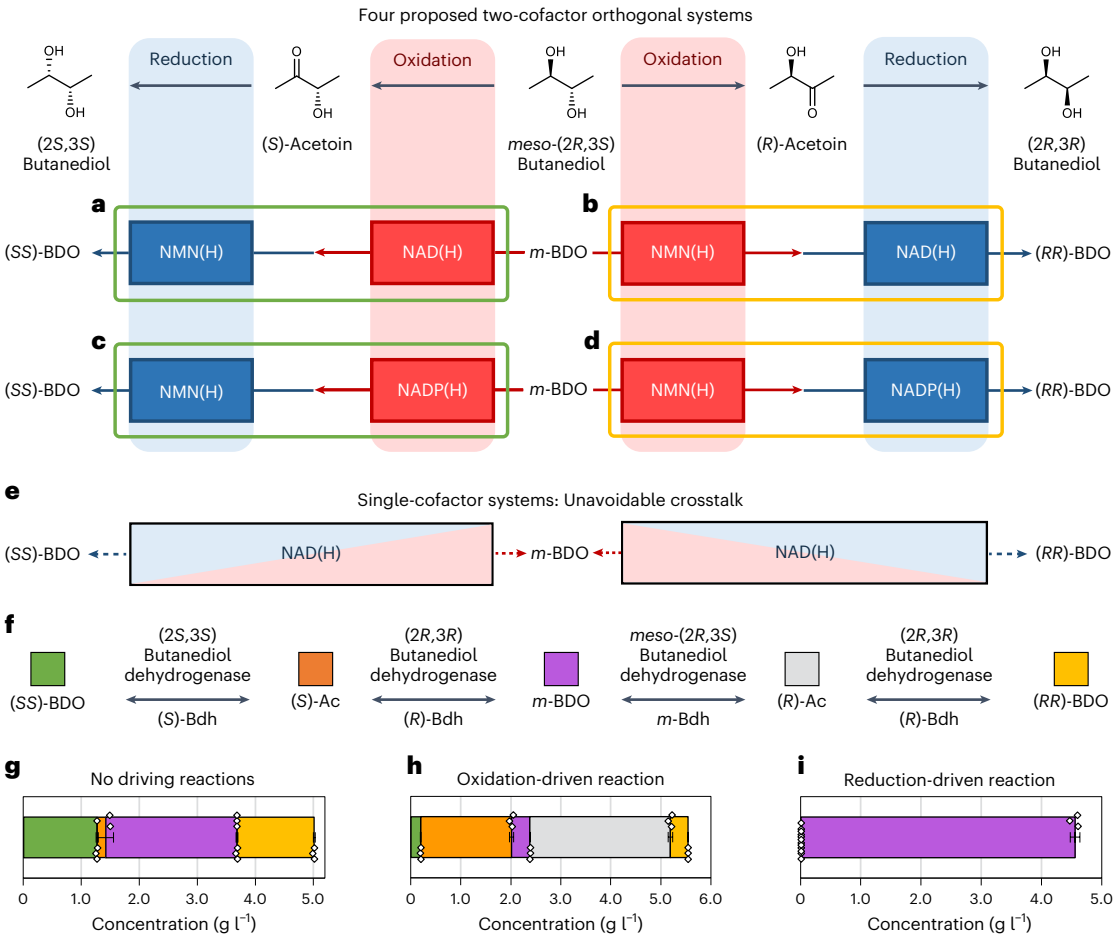

Fig. 1 | Overview of the four proposed BDO stereo-upgrading systems for testing the crosstalk of two orthogonal cofactors. a,**c**, Stereo-upgrading systems of *m*-BDO to (*SS*)-BDO where NAD(H) (**a**) or NADP(H) (**c**) drives the oxidation step and NMN(H) drives the reduction step. **b**,**d**, Stereo-upgrading systems of *m*-BDO to (*RR*)-BDO where NMN(H) drives the oxidation step and NAD(H) (**b**) or NADP(H) (**d**) drives the reduction step. **e**, Illustration showing that, when crosstalk between the oxidation and reduction steps occurs, reactions are reversible and incomplete. The four systems above cannot be achieved with a single cofactor or multiple crosstalking cofactors. Red and blue signify oxidation and reduction, respectively. The two-color cofactor pool boxes represent crosstalk and fully reversible reaction steps. **f**, The typical stereospecificity and chiral substrate preference of Bdhs from different enzyme classes used. **g**, Single-cofactor reaction of the Bdhs with no cofactor-recycling reactions driving each step. **h**, Single-cofactor reaction with *L. brevis* Nox WT recycling NADH to NAD^+ to drive the oxidation step. **i**, Single-cofactor reaction with *B. subtilis* GDH WT recycling NAD^+ to NADH to drive the reduction step. The reaction does not proceed past the first oxidation step. The substrate for all experiments is 5 g l^{-1} *m*-BDO and conversion is measured after 48 h at 30 °C. Bars represent the mean of three independent replicates with error bars of one s.d. White diamonds indicate the values of individual replicates.

improved activity compared to WT with NMNH (Supplementary Fig. 1a). This substitution is further discussed below.

With *Ll* Nox I159T as template, we next sought to further improve NMNH activity by using a high-throughput, growth-based selection platform[28] (Fig. 2a). This is based on an engineered *E. coli* strain MX502 (BW25113 *ΔpncC Δpgi Δzwf ΔnadR Δgnd* + pLM106 + pLS502)[28] (Supplementary Table 1) that metabolizes glucose exclusively by GDH Ortho, which relies on an NMNH-oxidizing enzyme for continuous function through the Entner–Doudoroff (ED) pathway instead of the conventional Embden–Meyerhof–Parnas (EMP) and the pentose phosphate pathways. Although this selection is not explicitly designed to yield orthogonal NMNH oxidases, we hypothesized that orthogonal Nox variants would stand out in the evolution because they would not disturb the NAD(P)H pools essential for cell fitness and they can turn over NMNH more rapidly without NAD(P)H occupying their active sites as competitive substrates.

During growth selection, three positions (D178, A179, and I243) were subjected to site-saturated mutagenesis with degenerate codons (NNK). These conserved sites had a demonstrable effect on the cofactor preference of *Lp* Nox[28]. The library yielded ~2×10^6 independent transformants, sufficient to cover the theoretical library size, $20^3 = 8{,}000$, by more than ten times. Selection was performed at 30 °C on agar plates of M9 minimal medium supplemented with 20 g l^{-1} D-glucose and 2 mM NMN^+. Plates were monitored for 10 days and 18 colonies were chosen for analysis on the basis of desirable growth phenotypes[28] compared to controls (Supplementary Table 1). A specific activity assay was performed on sequenced variants (Supplementary Table 2 and Supplementary Fig. 1b). The best variant *Ll* Nox I159T;D178N;A179F;I243E (Nox Ortho; Supplementary Table 1) demonstrated a ~250-fold increase in the apparent catalytic efficiency, k_{cat}/K_m, toward NMNH (Fig. 2b and Supplementary Fig. 2c). Consistent with our hypothesis, Nox Ortho also had the most severely diminished NADH activity, a ~100-fold decrease in apparent catalytic efficiency compared to WT (Fig. 2b, Supplementary Table 3 and Supplementary Fig. 2c). Catalytic efficiency toward NADPH remained low for both WT and Ortho (Fig. 2b, Supplementary Table 3 and Supplementary Fig. 2c).

To understand Nox Ortho's drastically switched cofactor preference, Rosetta docking was performed[51]. The resultant models suggested that the I159T substitution stabilizes NMNH binding by

https://doi.org/10.1038/s41589-024-01702-5

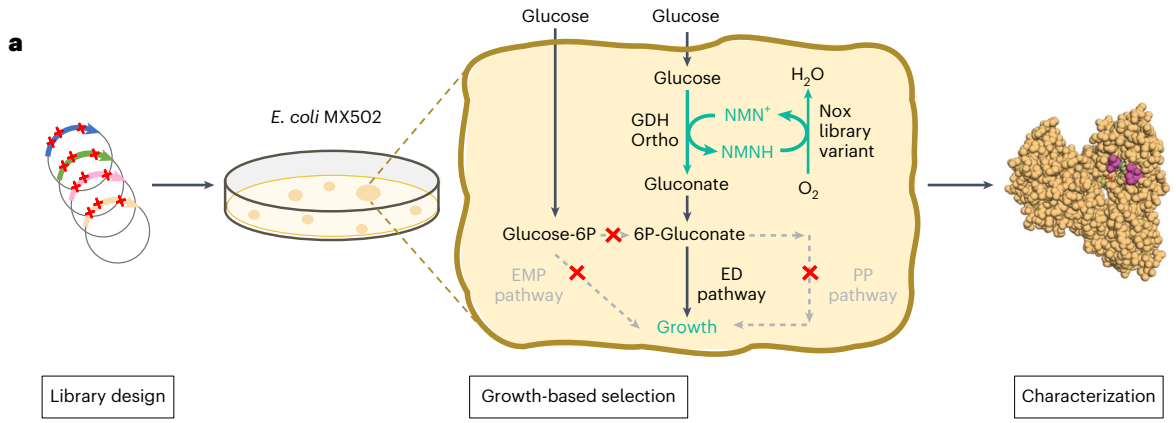

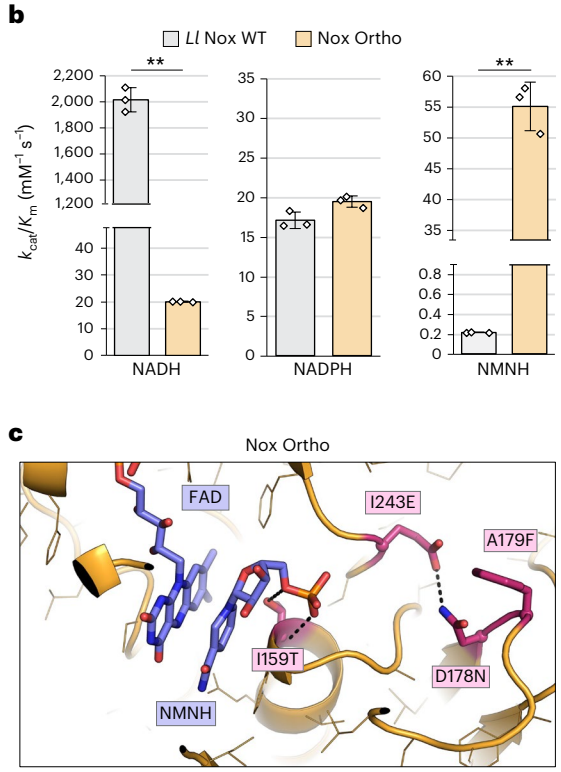

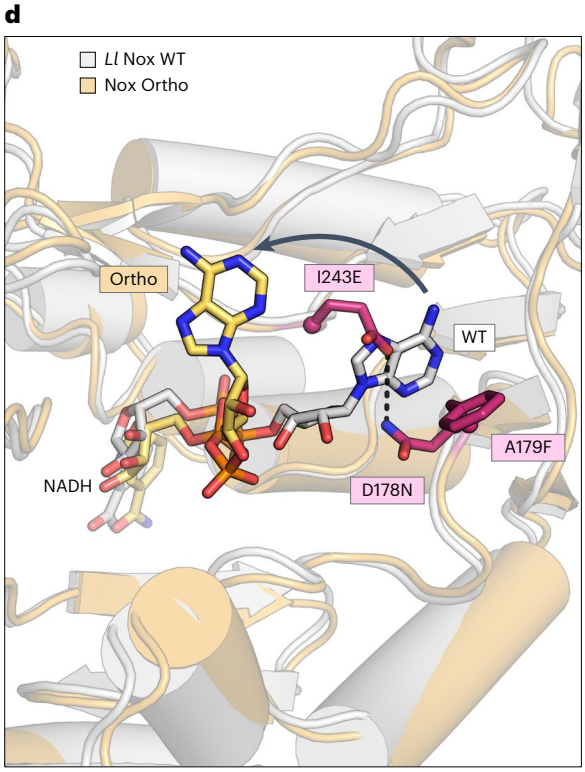

Fig. 2 | Directed evolution of *Ll* Nox to exclude NADH. a, Schematic of the high-throughput growth-based selection platform workflow for NMNH-using enzymes. The designed site-saturated mutagenesis library was introduced to the engineered *E. coli* strain MX502, where growth depends upon Nox NMNH oxidase activity through the ED pathway. Fast-growing variants were characterized by a specific activity assay. PP, pentose phosphate. **b**, The apparent catalytic efficiencies of *Ll* Nox WT (gray) and Nox Ortho (yellow) toward NADH, NADPH and NMNH. The assay was performed at 37 °C in 50 mM Tris-Cl pH 7.0 with varying concentrations of reduced cofactors. **c**, Model of Nox Ortho binding pose with NMNH and FAD revealed novel hydrogen-bond formation. **d**, *Ll* Nox WT (gray) and Nox Ortho (yellow) with NADH bound revealed a conformational change in NADH-binding pose. Substitutions on Nox Ortho exclude NADH from its native binding mode to become exposed to solvent, consistent with the decreased catalytic efficiency for NADH observed. Data are presented as the mean of three independent replicates ($n = 3$) with error bars of one s.d. White diamonds represent individual replicates. Two-tailed *t*-tests of unpaired samples were conducted assuming unequal variances (**$P < 0.01$): *Ll* Nox WT versus *Ll* Nox Ortho (NADH, $P = 0.00073$; NMNH, $P = 0.0017$).

introducing a novel polar interaction with the phosphate of NMNH, which was not seen when *Ll* Nox WT was modeled with NMNH (Fig. 2c and Supplementary Fig. 3). Taking these docking models as input, molecular dynamics (MD) simulations were conducted to further examine NMNH-binding stability in *Ll* Nox WT and Nox Ortho (Supplementary Fig. 4). The evolution of hydrogen bonds formed between the phosphate of NMNH and each enzyme over time was evaluated (Supplementary Fig. 4a,b) and we observed that Nox Ortho established more hydrogen bonds with NMNH than *Ll* Nox WT during the last 60 ns of the MD simulation (Supplementary Fig. 4c). While the number of hydrogen bonds formed by *Ll* Nox WT fluctuated between zero and one, Nox Ortho established two, three and occasionally four hydrogen bonds. This indicates an enhanced hydrogen-bond network at the Nox Ortho active site that supports NMNH stabilization.

D178N and I243E are predicted to form a new hydrogen bond (Fig. 2c,d). A179F potentially restricts the conformer choices of D178N, making the latter sample the hydrogen-bonding conformation more frequently (Fig. 2c,d). This hydrogen bond is predicted to dislodge NADH from the binding pocket into solvent (Fig. 2d). This prediction is supported by the high K_m of Nox Ortho for NADH and NADPH, as these natural cofactors lose contact with the binding pocket (Supplementary Table 3 and Supplementary Fig. 2c; a high K_m is inferred by nonsaturation kinetics at 2 mM reduced cofactor). Furthermore, at physiological concentrations of NADH and NADPH in *E. coli* (~0.1 – 1 mM)[52],

https://doi.org/10.1038/s41589-024-01702-5

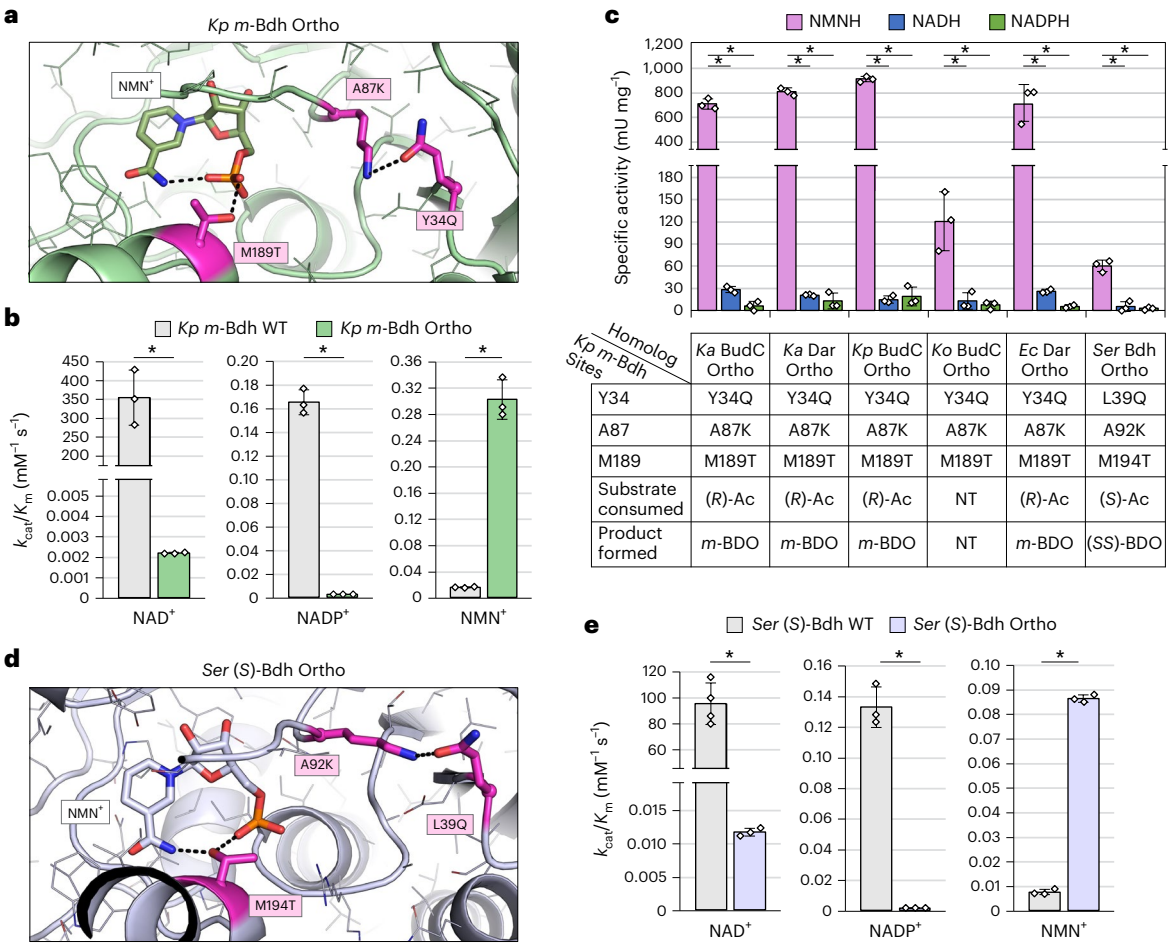

Fig. 3 | Engineering Bdhs to use NMN(H). a, Predicted interactions of *Kp m*-Bdh Ortho with NMN^+. **b**, Apparent catalytic efficiencies of *Kp m*-Bdh WT (gray) and *Kp m*-Bdh Ortho (green) with each cofactor. The substrate was 50 mM *m*-BDO with varying cofactor concentration. **c**, Specific activities of six Bdh homologs based on analogous substitution transfer from *Kp m*-Bdh Ortho (*Kp m*-Bdh sites). Summary of measured chiral substrate and product preference in (*R*/*S*)-Ac feeding experiments (Supplementary Fig. 6). NT, not tested. The substrate was 10 mM (*R*/*S*)-Ac with 0.2 mM reduced cofactor. One unit of enzymatic activity was defined as the quantity of enzyme required to consume 1 µmol of reduced cofactor (NADH, NADPH or NMNH) per minute. **d**, Predicted interactions of *Ser* (*S*)-Bdh Ortho with NMN^+. **e**, Apparent catalytic efficiencies of *Ser* (*S*)-Bdh WT (gray) and *Ser* (*S*)-Bdh Ortho (purple) with each cofactor. The substrate for *Ser* (*S*)-Bdh assays was 50 mM (*SS*)-BDO with varying cofactor concentration. Bars are the average of three independent replicates ($n = 3$) with error bars of one s.d. for all samples except for *Ser* (*S*)-Bdh WT with NAD^+ ($n = 4$). Individual replicates are shown as white diamonds. All activity assays of Bdhs were conducted at 30 °C in 50 mM Tris-Cl at pH 8.0. Two-tailed *t*-tests of unpaired samples were conducted assuming unequal variances (*$P < 0.05$): WT versus Ortho catalytic efficiency (*Kp m*-Bdh: NAD^+, $P = 0.014$; $NADP^+$, $P = 0.0014$; NMN^+, $P = 0.0037$; *Ser* (*S*)-Bdh: NAD^+, $P = 0.0012$; $NADP^+$, $P = 0.0033$; NMN^+, $P = 2.0 \times 10^{-7}$); NMNH versus NADH specific activity ($P = 0.0012$, 0.00049, 0.00010, 0.035, 0.015 and 0.00079); NMNH-specific versus NADPH-specific activity ($P = 0.00096$, 0.00013, 4.4×10^{-6}, 0.037, 0.014 and 0.0041).

the high K_m of Nox Ortho toward NADH and NADPH would imply that NAD(P)H occupies a small fraction of Nox Ortho active sites during the growth selection.

Reducing the size of the cofactor-binding pocket is an established approach to engineering enzymes to use smaller, noncanonical cofactors[27–29,53,54]. In our previous work engineering *Lp* Nox and phosphite dehydrogenase (Ptdh), bulky and hydrophobic residues were selected for at these conserved sites, which packed against one another to fill the cofactor-binding pocket and improve activity[28,29]. Those packing interactions, in principle, should introduce the same steric hindrance as the hydrogen bond discovered here. Yet, those hydrophobic packing substitutions did not effectively block NAD(H) and NADP(H) binding like the hydrogen bond in Nox Ortho. One explanation may be that a hydrogen bond is stronger than a van der Waals contact, making the steric hindrance more durable to enzyme conformational shifts during catalysis. Alternatively, when hydrophobic substitutions fill the cofactor-binding pocket instead of polar contacts, the residual interaction between the hydrophobic surface of the flexible adenylyl moiety and the hydrophobic cleft can persist.

Development of NMN(H)-specific Bdhs

With GDH Ortho and Nox Ortho in hand, we next needed Bdhs that can alter the (*S*)-chiral center using NMN(H) specifically (Fig. 1a–d).

For a Bdh that uses NMN(H) as the oxidizing cofactor (Fig. 1b,d), we chose the *m*-BDO dehydrogenase from *Klebsiella pneumoniae*, *Kp m*-Bdh, for its (*S*)-stereospecificity[55] and high expression. Following the design principle derived from Nox Ortho engineering, we created the NMN(H)-specific variant *Kp m*-Bdh Ortho, a triple mutant (M189T;Y34Q;A87K). We predicted that M189T would establish a novel polar contact with the phosphate of NMN^+ and that Y34Q and A87K would form a hydrogen bond to close off the binding pocket and prevent entry of $NAD(P)^+$ (Fig. 3a and Supplementary Fig. 5). This design was successful; the apparent catalytic efficiency of *Kp m*-Bdh Ortho for NMN^+ improved ~19-fold compared to WT (Fig. 3b, Supplementary Table 3 and Supplementary Fig. 2a). *Kp m*-Bdh Ortho's catalytic

https://doi.org/10.1038/s41589-024-01702-5

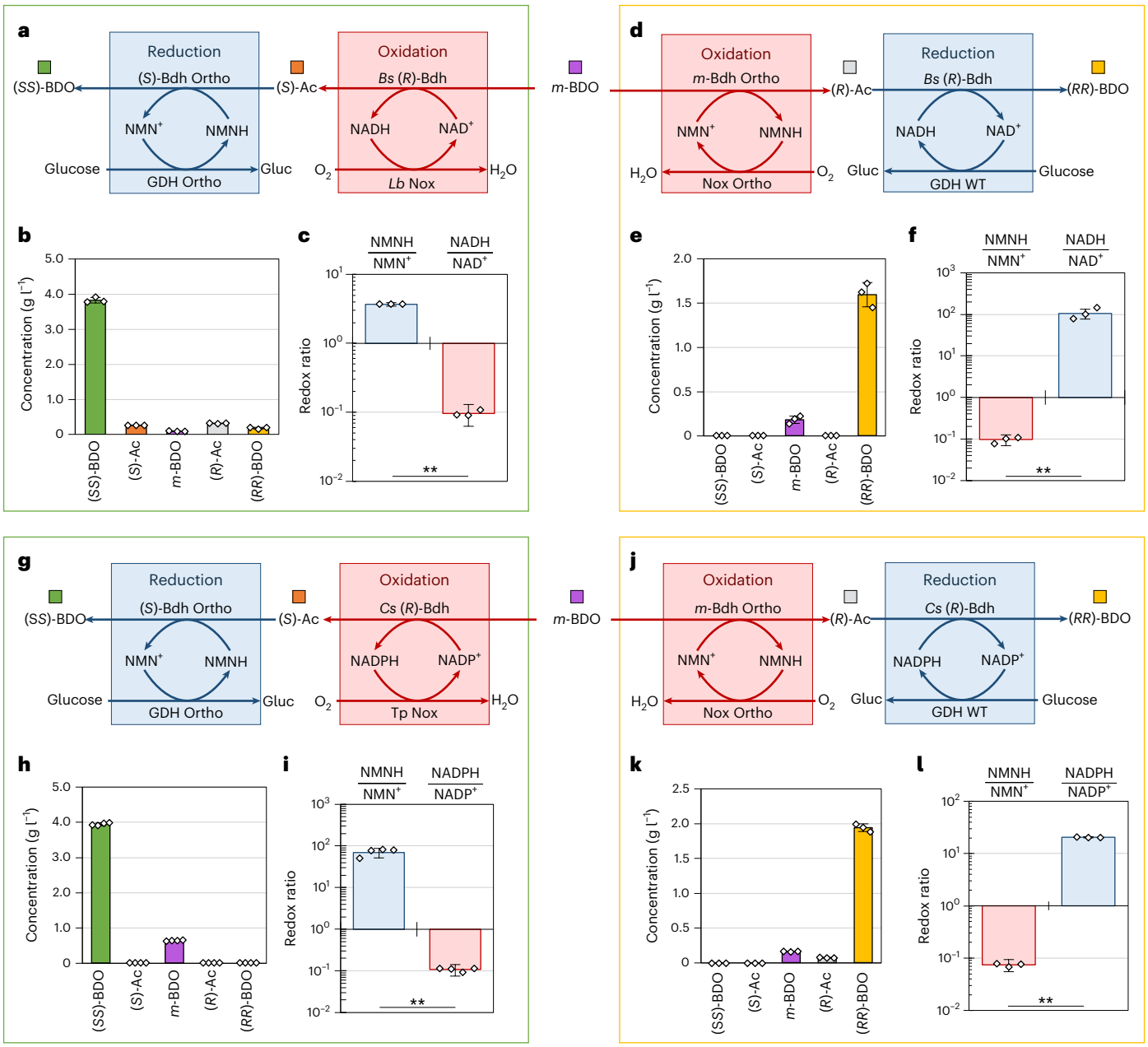

Fig. 4 | Orthogonal redox driving forces enable BDO stereo-upgrading in four cell-free systems. a–**c**, *m*-BDO to (*SS*)-BDO system that pairs an NAD(H)-driven oxidation step and NMN(H)-driven reduction step. **d**–**f**, *m*-BDO to (*RR*)-BDO system that pairs an NMN(H)-driven oxidation step and NAD(H)-driven reduction step. **g**–**i**, *m*-BDO to (*SS*)-BDO system that pairs an NADP(H)-driven oxidation step and NMN(H)-driven reduction step. **j**–**l**, *m*-BDO to (*RR*)-BDO system that pairs an NMN(H)-driven oxidation step and NADP(H)-driven reduction step. **a**,**d**,**g**,**j**, Reaction pathway maps. **b**,**e**,**h**,**k**, Concentration of BDO and Ac isomers. Samples were taken for gas chromatography (GC) at 24 h, 72 h, 72 h and 72 h, respectively. Bars represent the mean concentration of three or four independent replicates with error bars of one s.d. Individual replicates are shown as white diamonds. **c**,**f**,**i**,**l**, Concentration ratio of each redox cofactor's cognate reduced and oxidized species on a $\log_{10}$ scale. Samples were taken for redox ratio measurement at 48 h, 72 h, 48 h and 24 h, respectively. Samples for GC and redox ratio analysis were taken from the same reactions. Bars represent the ratio of concentration means for three or four independent replicates as depicted with error bars calculated by the propagation of error from the s.d. of oxidized and total cofactor concentration measurements. White diamonds represent the values of individually calculated replicates. Ortho represents the cofactor engineered variants. Gluc, gluconic acid. Two-tailed *t*-tests for paired samples of logarithm-transformed redox ratios were conducted assuming unequal variances (**$P < 0.01$): NMN(H) versus NAD(H) ratio to produce (*SS*)-BDO ($P = 0.00027$) and (*RR*)-BDO ($P = 0.00024$); NMN(H) versus NADP(H) ratio to produce (*SS*)-BDO ($P = 0.000023$) and (*RR*)-BDO ($P = 0.000055$).

efficiency for NAD^+ and $NADP^+$ decreased 1.6×10^5-fold and 70-fold compared to WT, respectively. Together, *Kp m*-Bdh Ortho features a 3.0×10^6-fold and 1.3×10^3-fold cofactor specificity switch compared to WT from NAD^+ or $NADP^+$ to NMN^+, respectively, by catalytic efficiency (Supplementary Table 3 and Supplementary Fig. 2a). Bdh and Nox share little homology (~13% pairwise sequence identity) and are vastly different structurally. Success in engineering distinct enzyme families suggests that our design rules are remarkably universal. Current efforts in our lab continue to broaden the classes of enzymes that these rules can be applied to.

Kp m-Bdh Ortho catalyzes the interconversion of *m*-BDO and (*R*)-Ac. For a Bdh that uses NMNH for reduction (Fig. 1a,c), our process requires that it accepts (*S*)-Ac as substrate to install an (*S*)-chiral center. To address this, we searched for six (*S*)-installing Bdhs from the

m-Bdh and (*S*)-Bdh enzyme families from the literature or by putative annotation: *K. aerogenes* KCTC 2190 BudC, *K. aerogenes* NCTC 8846 Dar, *K. pneumoniae* BudC[56], *K. oxytoca* KCTC 1686 BudC, *E. cloacae* ssp. *dissolvens* SDM Dar[57] and *Serratia* sp. AS13 (ref. 58) (Supplementary Tables 1, 4, and 5). We converted all of them into NMN(H)-orthogonal enzymes en masse by mapping the same substitution pattern as applied to *Kp m*-Bdh Ortho onto them (six successful transfers; Fig. 3c). This streamlined process again underscores the translatability of the design. We tested all variants by purified protein cycling reactions with NMN^+ (Supplementary Fig. 6a). All variants tested exhibit (*S*)-installing stereospecificity (Fig. 3c and Supplementary Fig. 6b,c), while only *Ser* Bdh Ortho (L39Q;A92K;M194T) showed the desired substrate preference converting (*S*)-Ac into (*SS*)-BDO. We renamed this variant *Ser* (*S*)-Bdh Ortho.

Rosetta modeling of *Ser* (*S*)-Bdh Ortho supports the prediction that the hydrogen bond formed by A92K and L39Q, while not affecting NMN^+ binding (Fig. 3d), pushes NAD^+ into a solvent-exposed, nonproductive binding pose (Supplementary Fig. 7). Furthermore, M194T anchors NMN^+ by interacting with its phosphate (Fig. 3d). Corroborating these predictions, *Ser* (*S*)-Bdh Ortho (L39Q;A92K;M194T) features an 8.7×10^4-fold and 1.0×10^3-fold cofactor specificity switch compared to WT from NAD^+ and $NADP^+$ to NMN^+, respectively, according to its apparent catalytic efficiency (Fig. 3e, Supplementary Table 3 and Supplementary Fig. 2b).

Overall, we obtained all necessary parts of the four BDO stereo-upgrading systems (Fig. 1a–d): GDH Ortho to generate NMNH-reducing power, Nox Ortho to generate NMN^+-oxidizing power and *Kp m*-Bdh Ortho and *Ser* (*S*)-Bdh Ortho to harness these orthogonal driving forces to manipulate (*S*)-chiral centers.

Orthogonal driving forces enable stereo-upgrading in vitro

Using the NMN(H)-specific enzymes, we tested all four designs systematically (Fig. 1a–d) using purified proteins in vitro (Fig. 4). GDH WT was used to reduce $NAD(P)^+$ and GDH Ortho was used to reduce NMN^+. *L. brevis* Nox (*Lb* Nox)[37], Tp Nox (an *Lb* Nox mutant; Supplementary Table 1)[41] and Nox Ortho were used to oxidize NADH, NADPH, and NMNH, respectively. Bdhs of appropriate cofactor, substrate, and chiral specificity were chosen accordingly (Supplementary Tables 4 and 5). Natural cofactors, $NAD(P)^+$, were supplemented at 2 mM or 0.2 mM (Methods) and NMN^+ was supplemented at 2 mM. All systems behaved as intended and demonstrated NMN(H)'s distinct reduction potential compared to NAD(H) and NADP(H) in either oxidizing or reducing directions based on the redox ratio.

In the system that included *Lb* Nox, *Bacillus subtilis* (*R*)-Bdh (*Bs* (*R*)-Bdh)[59], GDH Ortho, and *Ser* (*S*)-Bdh Ortho (Figs. 4a and 1a), 5 g l^{-1} *m*-BDO was converted to ~3.8 g l^{-1} (*SS*)-BDO (77% conversion) (Fig. 4b). Here, NMN(H) provided the reducing power and we observed a high NMNH:NMN^+ ratio at 3.7 ± 0.2 (Fig. 4c), while NADH:NAD^+ was maintained at a low ratio of 0.10 ± 0.03. Alternatively, in the system with Nox Ortho, *Kp m*-Bdh Ortho, GDH WT and *Bs* (*R*)-Bdh (Figs. 4d and 1b), 2 g l^{-1} *m*-BDO was converted to ~1.6 g l^{-1} (*RR*)-BDO (90% conversion) (Fig. 4e). Here, NMN(H) provided the oxidizing power with a low NMNH:NMN^+ ratio of 0.10 ± 0.03 versus NADH:NAD^+ at 100 ± 30 (Fig. 4f). Both systems achieved high purity in producing the desired BDO isomers. The stark contrast between NMN(H) and NAD(H) redox ratios supports that these two cofactors are orthogonal to each other.

The further the distance between the two cofactors' redox ratios, the more strongly they can deliver two opposing, insulated driving forces; this insulation is ensured by all enzymes' strict cofactor specificities. Indeed, when comparing the (*SS*)-BDO-producing system (Figs. 4a–c and 1a) to the (*RR*)-BDO-producing system (Figs. 4d–f and 1b), we observed that the closer NMN(H) versus NAD(H) redox ratios in the (*SS*)-BDO-producing system resulted in *Bs* (*R*)-Bdh and *Ser* (*S*)-Bdh Ortho retaining small residual ability to catalyze the reverse, unintended reactions, as evident by the slight buildup of side products (*RR*)-BDO, (*R*)-Ac and (*S*)-Ac. This could be because of the small side activity of *Ser* (*S*)-Bdh Ortho toward NAD^+ (Fig. 3e and Supplementary Table 3), which penetrates the insulation and permits some slow leakage by crosstalk between reactions. This was not observed in the system based on *Kp m*-Bdh Ortho paired with NAD(H) (Figs. 4d–f and 1b), which had superior specificity for NMN^+ (Fig. 3b and Supplementary Table 3). This leakage phenomenon because of crosstalk between reactions by shared cofactor usage exists and is shown to be prevalent and profound between the natural cofactors, NAD(H) and NADP(H), in nature because of the presence of numerous promiscuous enzymes[38] and the dynamic use of direct and indirect modes of cofactor exchange[6,39,41,42,60]. The high structural deviancy of noncanonical cofactors promises to mitigate this.

After showcasing our BDO stereo-upgrading system's capacity to orchestrate redox driving forces in complex mixtures using NAD(H) and NMN(H), we next sought to demonstrate that these principles are translatable to systems based on the other natural redox driving force, NADP(H), and thereby compatible with implementation in vivo. A system using NADP(H) paired with NMN(H) was also prepared. Previous studies described NADPH-dependent (*R*)-Bdhs[59,61,62] but we found their activity in *m*-BDO oxidation to be limited. Therefore, we bioprospected an $NADP^+$-active (*R*)-Bdh from *Clostridium saccharoperbutylacetonicum* (*Cs* (*R*)-Bdh) on the basis of sequence homology to the readily reversible *Bs* (*R*)-Bdh (Supplementary Fig. 8a–c). We subsequently confirmed specific activity with $NADP^+$ and stereospecific oxidation to destroy the (*R*)-chiral center of *m*-BDO (Supplementary Fig. 8d–g).

The (*SS*)-BDO-producing system contained Tp Nox, *Cs* (*R*)-Bdh, GDH Ortho and *Ser* (*S*)-Bdh Ortho (Fig. 4g) and produced ~3.9 g l^{-1} (*SS*)-BDO from 5 g l^{-1} *m*-BDO (86% conversion) (Fig. 4h). The redox ratios suggest that NMN(H) can be held far from equilibrium with NADP(H), with NMNH serving as a strong reducing power (NMNH:NMN^+ = 70 ± 20) (Fig. 4i), while the NADP(H) pool stays oxidized at 0.11 ± 0.03 (Fig. 4i). Unlike the (*SS*)-BDO-producing system based on NAD(H) (Fig. 4a), the NAD(P) system (Fig. 4g) does not suffer byproduct formation, consistent with the *Ser* (*S*)-Bdh Ortho's superior orthogonality toward $NADP^+$ (Fig. 3b, Supplementary Table 3 and Supplementary Fig. 2b). The complementary stereo-upgrading system contained Nox Ortho, *Kp m*-Bdh Ortho, GDH WT and *Cs* (*R*)-Bdh (Fig. 4j) and produced ~1.9 g l^{-1} (*RR*)-BDO from 2 g l^{-1} *m*-BDO (89% conversion) (Fig. 4k). Here, with NMN(H) as the oxidizing power, the NMNH:NMN^+ ratio was expectedly low (0.07 ± 0.02), while the reducing power in this system, NADP(H), was high (NADPH:$NADP^+$ = 20 ± 0.6) (Fig. 4l). These results demonstrate ideal orthogonality between NADP(H) and NMN(H) for the system based on *Kp m*-Bdh Ortho.

Altogether, *Kp m*-Bdh Ortho, *Ser* (*S*)-Bdh Ortho and Nox Ortho, which share a unifying enzyme design principle for cofactor specificity, combine to form four different stereo-upgrading systems capable of remarkedly pure preparations of chiral BDO.

NMN(H) enables BDO stereo-upgrading in *E. coli* whole cells

To convert *m*-BDO to (*SS*)-BDO, we started with a previously reported *E. coli* strain[12], MX102 R^0 (Supplementary Table 1). This cell cannot catabolize glucose, our sacrificial electron donor, and has decreased ability to degrade NMN^+ (refs. 12,63) (Fig. 5a). We first used NAD(H) as the oxidant and NMN(H) the reductant (Fig. 5b). *Lb* Nox, *Bs* (*R*)-Bdh, GDH Ortho, *Ser* (*S*)-Bdh Ortho and *Zymomonas mobilis* (*Zm* Glf) encoding a glucose transport facilitator were coexpressed from plasmids (Fig. 5b; pDA129, pDA131 and pSM10 in Supplementary Table 1) in *E. coli* and prepared as resting cells. When cells were incubated with 200 mM glucose, 5 g l^{-1} *m*-BDO and 10 mM NMN^+ supplemented, we were able to produce 3.8 g l^{-1} (*SS*)-BDO (Fig. 5c and Supplementary Fig. 9). The product purity of cells supplemented with 10 mM NMN^+ also increased dramatically relative to cells without NMN^+ supplementation, with the former reaching 81% pure (*SS*)-BDO (Fig. 5d). When no NMN^+ was supplemented, a substantial amount of (*S*)-Ac was observed. This is

https://doi.org/10.1038/s41589-024-01702-5

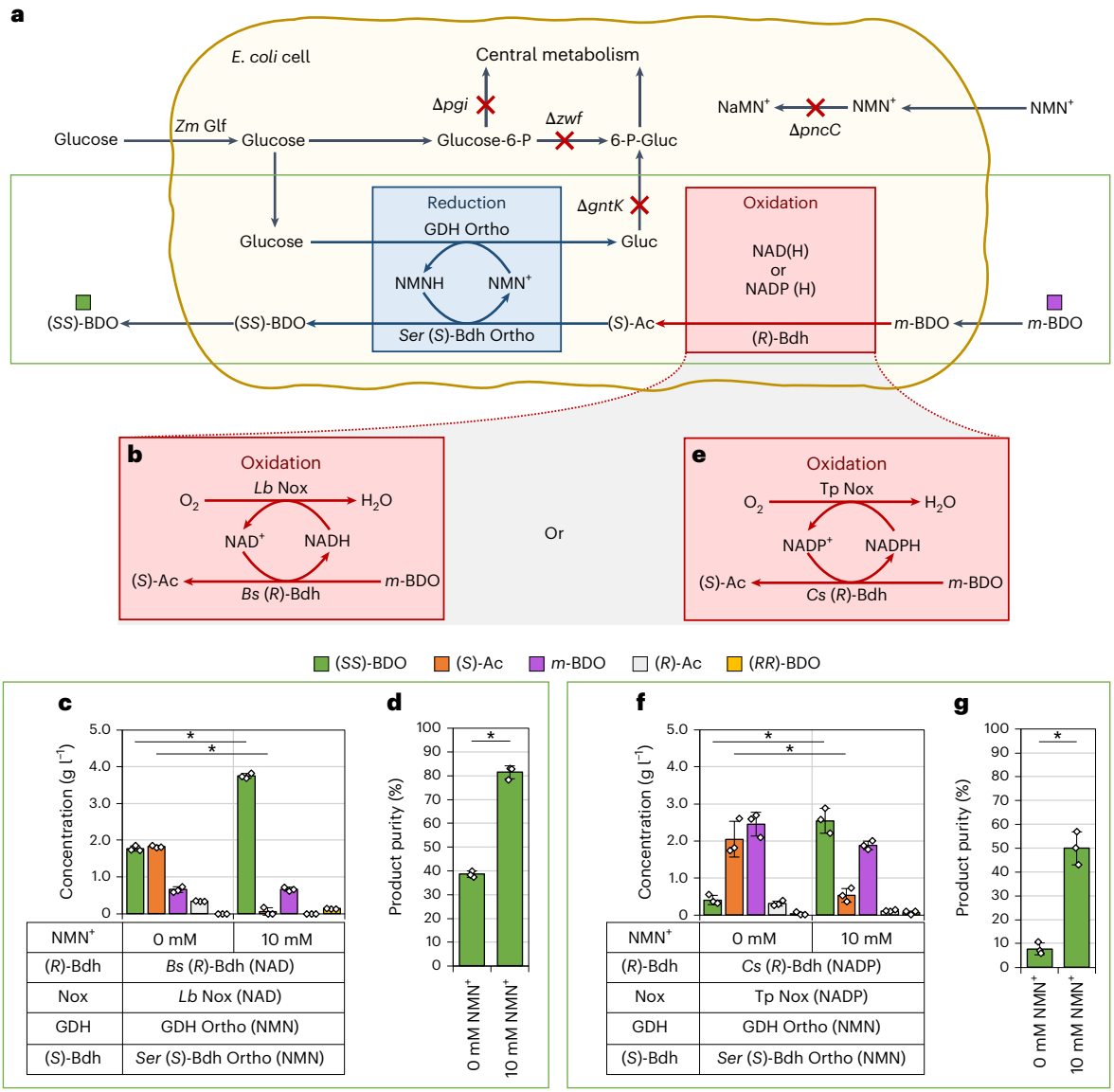

Fig. 5 | Resting cell stereo-upgrading of *m*-BDO to (*SS*)-BDO in *E. coli*. **a**, Gene deletions and reaction pathways in the whole-cell chassis, strain MX102 R^0. **b**–**d**, *m*-BDO to (*SS*)-BDO system using NAD(H)-driven oxidation step paired with an NMN(H)-driven reduction step in vivo. **b**, Reaction pathway details of the NAD(H)-driven oxidation step. **c**, Concentration of BDO and Ac stereoisomers when 0 mM or 10 mM NMN^+ was supplemented to the medium, sampled after 24 h at 30 °C. **d**, Product purity of (*SS*)-BDO in different NMN^+ supplementation conditions. **e**–**g**, *m*-BDO to (*SS*)-BDO system using NADP(H)-driven oxidation step paired with an NMN(H)-driven reduction step in vivo. **e**, Reaction pathway details of the NADP(H)-driven oxidation step. **f**, Concentration of BDO and Ac stereoisomers when 0 mM or 10 mM NMN^+ was supplemented to the medium, sampled after 152 h at 18 °C. **g**, Product purity of (*SS*)-BDO in different NMN^+ supplementation treatments. Bars represent an average of three biological replicates with error bars of one s.d. White diamonds represent the values of individual replicates. Two-tailed *t*-tests of paired samples were conducted assuming unequal variances ($P < 0.05$): effect of 0 mM versus 10 mM NMN^+ for (*SS*)-BDO and (*S*)-Ac percentage purity: **c**,**d**, $P = 0.0015$, 0.00047 and 0.0014; **f**,**g**, $P = 0.0078$, 0.016 and 0.0082. Product purity was calculated as the percentage of (*SS*)-BDO in the total amount of products formed ((*R*)-Ac, (*S*)-Ac, (*RR*)-BDO, (*SS*)-BDO and *m*-BDO). 6-P-Gluc, 6-phosphogluconate; Glucose-6P, glucose-6-phosphate; NaMN, nicotinic acid mononucleotide.

indicative of undesirable reversible reactions caused by insufficient driving forces, as discussed above.

The system can also function with NADP(H) as the oxidant, when *Lb* Nox is replaced with Tp Nox and *Bs* (*R*)-Bdh is replaced with *Cs* (*R*)-Bdh (Fig. 5e; pDA129, pDA162 and pSM10 in Supplementary Table 1). The resting cells produced a final titer of 2.5 g l^{-1} (*SS*)-BDO when 10 mM NMN^+ was supplied (Fig. 5f and Supplementary Fig. 10). Without NMN^+ supplementation, very little (*SS*)-BDO was produced (0.40 g l^{-1}) even though a high concentration of (*S*)-Ac was formed (2.0 g l^{-1}), suggesting a lack of reducing power when NMN^+ was not supplied. Again, the product purity in the NMN^+-supplied cells was greatly improved, from 7.7% pure with 0 mM NMN^+ to 50% pure (*SS*)-BDO with 10 mM NMN^+ (Fig. 5g). The primary impurity in this system was *m*-BDO, the starting material, which points to the first, oxidative step catalyzed by the NADP(H)-active *Cs* Bdh and driven by NADPH-specific Tp Nox as the major bottleneck. The equivalent cell-free system readily catalyzed the oxidation with $NADP^+$ (Fig. 4g–i). Yet, even in resting *E. coli* cells, the redox ratio of NADP(H) is challenging to invert toward efficient oxidation. The small total NADP(H) pool size could also impact the efficiency of this step; basal NADP(H) concentrations are on the order of 0.1 mM (ref. 52), whereas 2 mM $NADP^+$ was provided in the cell-free system (Fig. 4g–i).

https://doi.org/10.1038/s41589-024-01702-5

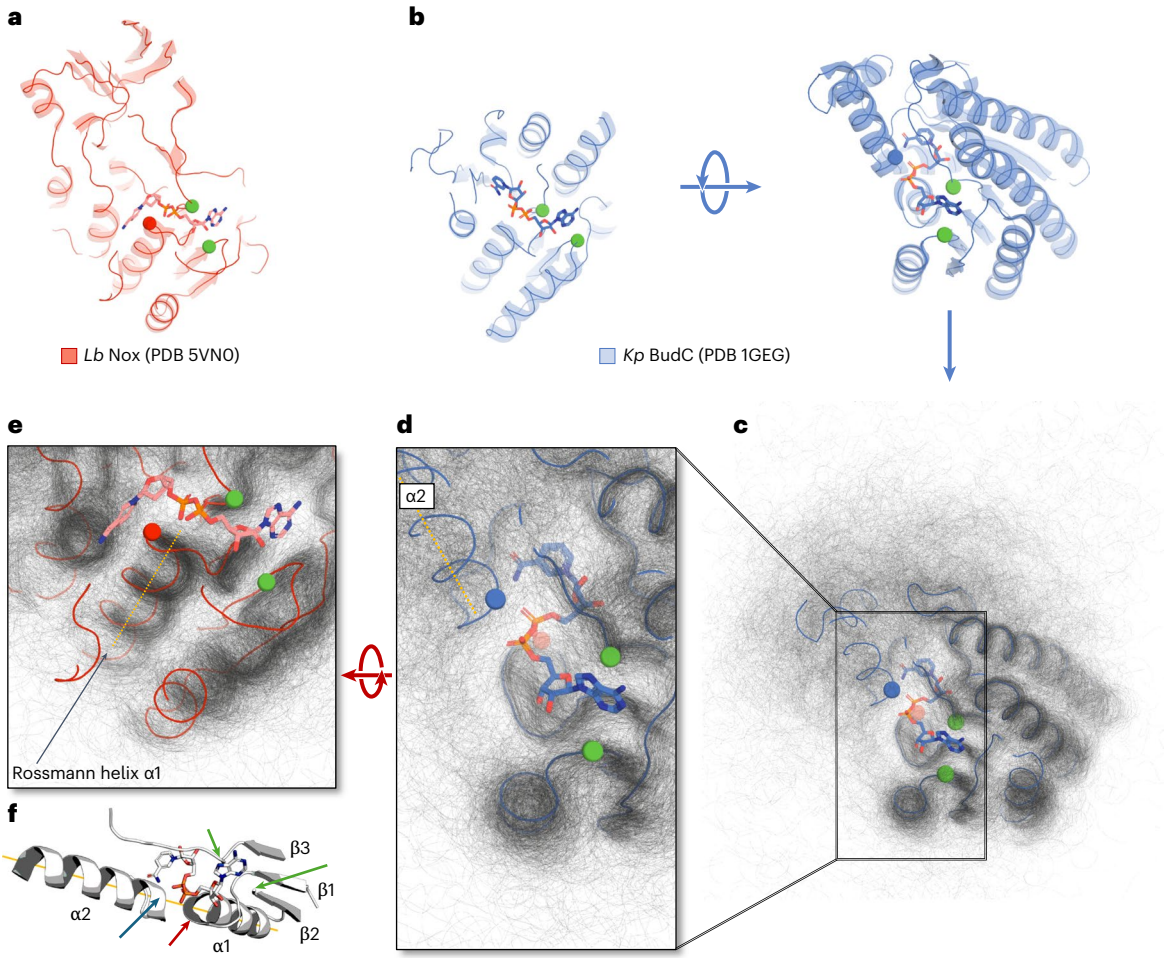

Fig. 6 | Visualizing emerging design principles for noncanonical redox cofactor-specific enzyme design. a,**b**, Alignment of previously experimentally resolved structures of Nox (**a**) and Bdh (**b**) that are similar to *Ll* Nox and *Kp* Dar, the enzymes engineered in this study (PDB 5VN0 and 1GEG, respectively). Green spheres represent the analogous sites substituted to block dinucleotide cofactors in Nox Ortho and Bdh Ortho. Red and blue spheres mark the site of substitution proposed to form an NMN(H) polar interaction. The rotated view of Bdh displays all three sites of mutagenesis. **c**, The same view of Bdh from **b** superimposed onto 617 members of its CATH superfamily. Dark regions result from multiple overlapping structures and are interpreted as a metric for structurally conserved backbone positions. **d**, Magnified image of the substitutions present in Bdh Ortho. Helix α2 is highlighted as a promising design region and is roughly coaxial to Rossmann helix α1. **e**, The original view of Nox is aligned to the CATH superposition model with the Nox backbone trace highlighted in red. Substitution I159T on Rossmann helix α1 is marked with a red sphere. The α1 axis is highlighted with a yellow line. **f**, A minimal Rossmann motif of Bdh (PDB 1GEG) is annotated with coaxial helix axes and arrows as a reference for previously described sites of design.

Orthogonal metabolic systems can vastly simplify the optimization efforts required to achieve whole-cell biotransformation because the engineering efforts are focused on the heterologous pathway itself. However, the approach of orthogonal metabolic systems still relies upon what is presently specialized expertise in engineering enzymes for noncanonical cofactors; broad adoption of this versatile strategy to control metabolic flux hinges on the capability of a range of users to translate successful designs across the diverse biocatalytic repertoire that exists in nature.

Mapping design principles onto the Rossmann superfamily

In the design of *m*-Bdh Ortho and (*S*)-Bdh Ortho, we observed that paired substitutions, predicted to form a polar contact that interrupts dinucleotide binding, translated amongst enzymes with low sequence homology (Supplementary Fig. 12a). Yet, structural homology among these enzymes does occur at the Rossmann fold[64–66]. We sought to map our substitutions against Rossmann-fold-containing proteins that represent a diverse sequence and functional space.

First, we located the equivalent substitution sites of Nox Ortho and *m*-Bdh Ortho on their homologs, *L. brevis* Nox (Protein Data Bank (PDB) 5VN0)[41] and *Kp* BudC (PDB 1GEG)[56], respectively (Fig. 6a,b, red, green and blue spheres). The substitutions described as blocking dinucleotide cofactors are represented with green spheres. The substitutions described as hydrogen-bonding partners to the terminal phosphate of NMN(H) are represented with red or blue spheres.

Next, we sought to project the substitution signatures of Nox Ortho and *m*-Bdh Ortho (Fig. 6a,b, respectively) onto the broad NAD(P)-binding Rossmann-like domain superfamily in the CATH (class, architecture, topology, homology) database (CATH superfamily 3.40.50.720)[67] to understand site conservation. High conservation could indicate high generalizability of our design principles at these sites to build NMN^+-orthogonal enzymes. In total, 617 experimentally determined protein structures—each a discrete structural neighborhood representative within the superfamily—were systematically superimposed (Fig. 6c), with most sharing <30% pairwise sequence similarity (Supplementary Fig. 12b). Here, darkness of the backbone superposition was interpreted as a structural conservation metric, where darker regions are more conserved. Note that Nox Ortho's or *m*-Bdh Ortho's dinucleotide cofactor-blocking sites are in highly conserved areas (Fig. 6d,e), which correspond to loops adjacent to β2 and

β3 strands of the Rossmann fold (Fig. 6f). This suggests high translatability of the NAD(P)$^+$-excluding strategy reported here.

We also analyzed strategies reported here to enable NMN(H) activity, namely, novel polar interactions to NMN(H). We observed that I159T in Nox Ortho is in the highly conserved helix α1 in the Rossman fold (Fig. 6e, red sphere, with helical axis as a yellow line, and Fig. 6f, red arrow), consistent with our prior experimental success in this site's translatability[28,29].

Alternatively, targeting the site represented by M189T of *m*-BDO Ortho (Fig. 6d, blue sphere) has robustly yielded high-NMN$^+$-activity mutants across different proteins. This site was translated among all six NMN(H)-active Bdh variants reported here (M189T;M192T in Supplementary Table 3 and Figs. 3c and 6d), which share 47.3–99.6% sequence similarity (Supplementary Fig. 12a), and our previously engineered GDH Ortho[12] (position I195R). This site is located on a second α-helix coaxial to Rossmann helix α1 (Fig. 6d, yellow line, and Fig. 6f, α2). This area is less conserved because it is peripheral to the core Rossmann domain (Fig. 6c,d). For enzyme scaffolds with this additional helix, we envision strong translatability of the design principle based on this site to build polar contacts to NMN$^+$.

Altogether, the design principles emerging from this work, which may be translated to a broad range of enzymes, are twofold. First, NMN(H) recognition can be initiated using sites on Rossmann helix α1 or α2 (Fig. 6). Second, NAD(H) and NADP(H) can be excluded by closing the space between Rossmann strands β2 and β3 (Fig. 6).

Conclusion

This work uncovered an enzyme design principle (polar contacts that bridge across the cofactor-binding pocket) as a reliable strategy to engineer NMN(H)-orthogonal biocatalysts. Parallel implementation of this design principle across diverse enzymes enables the construction of orthogonal metabolic systems. Here, we recreated one of the most important design principles in cellular metabolism, chemical compartmentalization by specific coenzymes[41,68], and quantified actual reduction potentials by the redox ratios of cofactors in our two-dimensional redox systems. The methodology presented here on a synthetic redox metabolism is true to the seminal description of orthogonal metabolic organization present in nature[68].

The ability to manipulate the thermodynamic equilibrium of select metabolic processes leveraging redox ratio with low interference from natural dehydrogenases[15] is an especially promising capability of NMN(H) as a noncanonical redox cofactor. We anticipate that this strategy, when protein engineering is streamlined, can be broadly enabling to the flexible biomanufacturing goals envisioned by metabolic engineers. Our ability to engineer enzymes for NMN(H) presently yields notably less catalytically efficient enzymes than their natural counterparts with the canonical cofactors[12,29,30]. Yet, with these enzymes, we are able to integrate these circuits into whole cells with minimal effort to balance redox resource allocation. Recent efforts in protein engineering enabled by directed evolution, machine learning and high-throughput screening have greatly accelerated the rate of enzyme design and we envisage that iteration upon these techniques will soon close this gap. As orthogonal redox enzymes improve, so do their derivative selection platforms and screening technologies.

For BDO stereo-upgrading specifically, the primary limitation to its economic viability is the rate of our present biocatalysts. Low catalytic efficiency requires more enzyme to be present, which decreases the economic viability of the process. However, if future research addresses these rates, then BDO stereo-upgrading pipelines could also be extended to resolve the lower-cost mixtures of all three BDO isomers into a single, value-added enantiomer. Of course, glucose as a sacrificial electron source as presented in our initial proof of concept is not a cost-effective substrate. Transition of the pathway to eventually rely on lower-cost substrates such as phosphite or formate would greatly improve the process economics but would require additional protein engineering on these biocatalysts. Eventually, these systems could also interface with natural or engineered BDO producers in coculture or be integrated into a single BDO producer by rewiring sugar use.

We show that the reduction potential of NMNH:NMN$^+$ is disconnected to that of NADH:NAD$^+$ and NADPH:NADP$^+$, in both cell-free preparations and *E. coli* whole cells. Partitioning and balancing redox cofactors are a prevalent need in metabolic engineering. Unlike NAD(P)$^+$, noncanonical cofactors are not tied to natural metabolism. Given that their recycling enzymes, such as GDH Ortho and Nox Ortho, can be expressed in the desired cellular compartment, with tunable level and at a controllable timing, noncanonical redox systems can support precise spatiotemporal control. Therefore, they may be deployed to solve the prevalent problem of balancing redox in metabolic engineering with a much wider range of freedom. This work presented the full infrastructure of using NMN$^+$ as an orthogonal redox cofactor with its designated electron source and electron sink. We demonstrated this concept using NMN(H) to direct unwavering redox driving forces using BDO stereo-upgrading as a proof of concept. Looking forward, access to intricate control of reduction potential in individual metabolic processes, in separate cellular or organ compartments, at the correct time and without interference with delicate global redox homeostasis is essential[37,60,69–72].

Online content

Any methods, additional references, Nature Portfolio reporting summaries, source data, extended data, supplementary information, acknowledgements, peer review information; details of author contributions and competing interests; and statements of data and code availability are available at https://doi.org/10.1038/s41589-024-01702-5.

References

1. Liu, Y. et al. Biofuels for a sustainable future. *Cell* **184**, 1636–1647 (2021).
2. Liao, J. C., Mi, L., Pontrelli, S. & Luo, S. Fuelling the future: microbial engineering for the production of sustainable biofuels. *Nat. Rev. Microbiol.* **14**, 288–304 (2016).
3. Opgenorth, P. H., Korman, T. P. & Bowie, J. U. A synthetic biochemistry molecular purge valve module that maintains redox balance. *Nat. Commun.* **5**, 4113 (2014).
4. Cresko, J. et al. *Industrial Decarbonization Roadmap* (US Department of Energy, 2022).
5. Lee, S. Y. & Kim, H. U. Systems strategies for developing industrial microbial strains. *Nat. Biotechnol.* **33**, 1061–1072 (2015).
6. Walsh, C. T., Tu, B. P. & Tang, Y. Eight kinetically stable but thermodynamically activated molecules that power cell metabolism. *Chem. Rev.* **118**, 1460–1494 (2018).
7. Zachos, I., Döring, M., Tafertshofer, G., Simon, R. C. & Sieber, V. carba nicotinamide adenine dinucleotide phosphate: robust cofactor for redox biocatalysis. *Angew. Chem. Int. Ed. Engl.* **60**, 14701–14706 (2021).
8. Beier, A. et al. Switch in cofactor specificity of a Baeyer–Villiger monooxygenase. *ChemBioChem* **17**, 2312–2315 (2016).
9. Chánique, A. M. & Parra, L. P. Protein engineering for nicotinamide coenzyme specificity in oxidoreductases: attempts and challenges. *Front. Microbiol.* **9**, 194 (2018).
10. Rollin, J. A., Tam, T. K. & Zhang, Y.-H. P. New biotechnology paradigm: cell-free biosystems for biomanufacturing. *Green Chem.* **15**, 1708 (2013).
11. Mampel, J., Buescher, J. M., Meurer, G. & Eck, J. Coping with complexity in metabolic engineering. *Trends Biotechnol.* **31**, 52–60 (2013).
12. Black, W. B. et al. Engineering a nicotinamide mononucleotide redox cofactor system for biocatalysis. *Nat. Chem. Biol.* **16**, 87–94 (2020).

13. Pandit, A. V., Srinivasan, S. & Mahadevan, R. Redesigning metabolism based on orthogonality principles. *Nat. Commun.* **8**, 1–11 (2017).
14. Wang, X. et al. Creating enzymes and self-sufficient cells for biosynthesis of the non-natural cofactor nicotinamide cytosine dinucleotide. *Nat. Commun.* **12**, 2116 (2021).
15. Richardson, K. N., Black, W. B. & Li, H. Aldehyde production in crude lysate- and whole cell-based biotransformation using a noncanonical redox cofactor system. *ACS Catal.* **10**, 8898–8903 (2020).
16. Bat-Erdene, U. et al. Cell-free total biosynthesis of plant terpene natural products using an orthogonal cofactor regeneration system. *ACS Catal.* **11**, 9898–9903 (2021).
17. Milo, R., Jorgensen, P., Moran, U., Weber, G. & Springer, M. BioNumbers—the database of key numbers in molecular and cell biology. *Nucleic Acids Res.* **38**, D750–D753 (2010).
18. Pan, X. et al. A genetically encoded tool to increase cellular NADH/NAD^+ ratio in living cells. *Nat. Chem. Biol.* **20**, 594–604 (2024).
19. Voss, C. V. et al. Orchestration of concurrent oxidation and reduction cycles for stereoinversion and deracemisation of *sec*-alcohols. *J. Am. Chem. Soc.* **130**, 13969–13972 (2008).
20. Liu, H. & Bowie, J. U. Cell-free synthetic biochemistry upgrading of ethanol to 1,3 butanediol. *Sci. Rep.* **11**, 9449 (2021).
21. Knaus, T., Cariati, L., Masman, M. F. & Mutti, F. G. In vitro biocatalytic pathway design: orthogonal network for the quantitative and stereospecific amination of alcohols. *Org. Biomol. Chem.* **15**, 8313–8325 (2017).
22. Drenth, J., Yang, G., Paul, C. E. & Fraaije, M. W. A tailor-made deazaflavin-mediated recycling system for artificial nicotinamide cofactor biomimetics. *ACS Catal.* **11**, 11561–11569 (2021).
23. Knaus, T. et al. Better than nature: nicotinamide biomimetics that outperform natural coenzymes. *J. Am. Chem. Soc.* **138**, 1033–1039 (2016).
24. Zachos, I. et al. Hot flows: evolving an archaeal glucose dehydrogenase for ultrastable carba-$NADP^+$ using microfluidics at elevated temperatures. *ACS Catal.* **12**, 1841–1846 (2022).
25. Campbell, E., Meredith, M., Minteer, S. D. & Banta, S. Enzymatic biofuel cells utilizing a biomimetic cofactor. *Chem. Commun.* **48**, 1898 (2012).
26. Guarneri, A. et al. Flavoenzyme-mediated regioselective aromatic hydroxylation with coenzyme biomimetics. *ChemCatChem* **12**, 1368–1375 (2020).
27. Meng, D. et al. Coenzyme engineering of glucose-6-phosphate dehydrogenase on a nicotinamide-based biomimic and its application as a glucose biosensor. *ACS Catal.* **13**, 1983–1998 (2023).
28. King, E. et al. Orthogonal glycolytic pathway enables directed evolution of noncanonical cofactor oxidase. *Nat. Commun.* **13**, 7282 (2022).
29. Zhang, L. et al. Directed evolution of phosphite dehydrogenase to cycle noncanonical redox cofactors via universal growth selection platform. *Nat. Commun.* **13**, 5021 (2022).
30. King, E. et al. Engineering Embden–Meyerhof–Parnas glycolysis to generate noncanonical reducing power. *ACS Catal.* **12**, 8582–8592 (2022).
31. Huang, R., Chen, H., Upp, D. M., Lewis, J. C. & Zhang, Y.-H. P. J. A high-throughput method for directed evolution of $NAD(P)^+$-dependent dehydrogenases for the reduction of biomimetic nicotinamide analogues. *ACS Catal.* **9**, 11709–11719 (2019).
32. Liang, K. & Shen, C. R. Selection of an endogenous 2,3-butanediol pathway in *Escherichia coli* by fermentative redox balance. *Metab. Eng.* **39**, 181–191 (2017).
33. Maina, S. et al. Prospects on bio-based 2,3-butanediol and acetoin production: recent progress and advances. *Biotechnol. Adv.* **54**, 107783 (2022).
34. Xiao, Z. et al. A novel whole-cell biocatalyst with NAD^+ regeneration for production of chiral chemicals. *PLoS ONE* **5**, e8860 (2010).
35. He, Y. et al. Efficient (3*S*)-acetoin and (2*S*,3*S*)-2,3-butanediol production from *meso*-2,3-butanediol using whole-cell biocatalysis. *Molecules* **23**, 691 (2018).
36. Zu, H. et al. Highly enantioselective synthesis of (*R*)-1,3-butanediol via deracemization of the corresponding racemate by a whole-cell stereoinverting cascade system. *Microb. Cell Fact.* **19**, 125 (2020).
37. Titov, D. V. et al. Complementation of mitochondrial electron transport chain by manipulation of the NAD^+/NADH ratio. *Science* **352**, 231–235 (2016).
38. Sellés Vidal, L., Kelly, C. L., Mordaka, P. M. & Heap, J. T. Review of NAD(P)H-dependent oxidoreductases: properties, engineering and application. *Biochim. Biophys. Acta Proteins Proteom.* **1866**, 327–347 (2018).
39. Jan, J., Martinez, I., Wang, Y., Bennett, G. N. & San, K. Y. Metabolic engineering and transhydrogenase effects on NADPH availability in *Escherichia coli*. *Biotechnol. Prog.* **29**, 1124–1130 (2013).
40. Weckbecker, A. & Hummel, W. Improved synthesis of chiral alcohols with *Escherichia coli* cells co-expressing pyridine nucleotide transhydrogenase, $NADP^+$-dependent alcohol dehydrogenase and NAD^+-dependent formate dehydrogenase. *Biotechnol. Lett.* **26**, 1739–1744 (2004).
41. Cracan, V., Titov, D. V., Shen, H., Grabarek, Z. & Mootha, V. K. A genetically encoded tool for manipulation of $NADP^+$/NADPH in living cells. *Nat. Chem. Biol.* **13**, 1088–1095 (2017).
42. Krebs, H. A. & Veech, R. L. Equilibrium relations between pyridine nucleotides and adenine nucleotides and their roles in the regulation of metabolic processes. *Adv. Enzym. Regul.* **7**, 397–413 (1969).
43. Wu, J. T., Wu, L. H. & Knight, J. A. Stability of NADPH: effect of various factors on the kinetics of degradation. *Clin. Chem.* **32**, 314–319 (1986).
44. Guarneri, A., van Berkel, W. J. & Paul, C. E. Alternative coenzymes for biocatalysis. *Curr. Opin. Biotechnol.* **60**, 63–71 (2019).
45. Nowak, C., Pick, A., Csepei, L.-I. & Sieber, V. Characterization of biomimetic cofactors according to stability, redox potentials, and enzymatic conversion by NADH oxidase from *Lactobacillus pentosus*. *ChemBioChem* **18**, 1944–1949 (2017).
46. Nowak, C. et al. A water-forming NADH oxidase from *Lactobacillus pentosus* suitable for the regeneration of synthetic biomimetic cofactors. *Front. Microbiol.* **6**, 957 (2015).
47. Zachos, I., Nowak, C. & Sieber, V. Biomimetic cofactors and methods for their recycling. *Curr. Opin. Chem. Biol.* **49**, 59–66 (2019).
48. Rasor, B. J., Yi, X., Brown, H., Alper, H. S. & Jewett, M. C. An integrated in vivo/in vitro framework to enhance cell-free biosynthesis with metabolically rewired yeast extracts. *Nat. Commun.* **12**, 5139 (2021).
49. Sudar, M., Findrik, Z., Domanovac, M. V. & Vasić-Rački, D. Coenzyme regeneration catalyzed by NADH oxidase from *Lactococcus lactis*. *Biochem. Eng. J.* **88**, 12–18 (2014).
50. Kim, S. & Hahn, J. S. Efficient production of 2,3-butanediol in *Saccharomyces cerevisiae* by eliminating ethanol and glycerol production and redox rebalancing. *Metab. Eng.* **31**, 94–101 (2015).
51. Richter, F., Leaver-Fay, A., Khare, S. D., Bjelic, S. & Baker, D. De novo enzyme design using Rosetta3. *PLoS ONE* **6**, e19230 (2011).
52. Bennett, B. D. et al. Absolute metabolite concentrations and implied enzyme active site occupancy in *Escherichia coli*. *Nat. Chem. Biol.* **5**, 593–599 (2009).

53. Wang, J. et al. Engineering formaldehyde dehydrogenase from *Pseudomonas putida* to favor nicotinamide cytosine dinucleotide. *ChemBioChem* **23**, 6–11 (2022).
54. Liu, Y. et al. Structural insights into phosphite dehydrogenase variants favoring a non-natural redox cofactor. *ACS Catal.* **9**, 1883–1887 (2019).
55. Li, J. X. et al. Enhanced production of optical (*S*)-acetoin by a recombinant *Escherichia coli* whole-cell biocatalyst with NADH regeneration. *RSC Adv.* **8**, 30512–30519 (2018).
56. Otagiri, M. et al. Crystal structure of *meso*-2,3-butanediol dehydrogenase in a complex with NAD^+ and inhibitor mercaptoethanol at 1.7 Å resolution for understanding of chiral substrate recognition mechanisms. *J. Biochem.* **129**, 205–208 (2001).
57. Li, L. et al. Biocatalytic production of (2*S*,3*S*)-2,3-butanediol from diacetyl using whole cells of engineered *Escherichia coli*. *Bioresour. Technol.* **115**, 111–116 (2012).
58. Zhang, L. et al. Mechanism of 2,3-butanediol stereoisomers formation in a newly isolated *Serratia* sp. T241. *Sci. Rep.* **6**, 19257 (2016).
59. Yan, Y., Lee, C.-C. & Liao, J. C. Enantioselective synthesis of pure (*R*,*R*)-2,3-butanediol in *Escherichia coli* with stereospecific secondary alcohol dehydrogenases. *Org. Biomol. Chem.* **7**, 3914 (2009).
60. Jones, D. P. & Sies, H. The redox code. *Antioxid. Redox Signal.* **23**, 734–746 (2015).
61. Nielsen, D. R., Yoon, S.-H., Yuan, C. J. & Prather, K. L. J. Metabolic engineering of acetoin and *meso*-2,3-butanediol biosynthesis in *E. coli*. *Biotechnol. J.* **5**, 274–284 (2010).
62. Liang, K. & Shen, C. R. Engineering cofactor flexibility enhanced 2,3-butanediol production in *Escherichia coli*. *J. Ind. Microbiol. Biotechnol.* **44**, 1605–1612 (2017).
63. Black, W. B. et al. Metabolic engineering of *Escherichia coli* for optimized biosynthesis of nicotinamide mononucleotide, a noncanonical redox cofactor. *Microb. Cell Fact.* **19**, 1–10 (2020).
64. Toledo-Patiño, S., Pascarelli, S., Uechi, G. & Laurino, P. Insertions and deletions mediated functional divergence of Rossmann fold enzymes. *Proc. Natl Acad. Sci. USA* **119**, e2207965119 (2022).
65. Rao, S. T. & Rossmann, M. G. Comparison of super-secondary structures in proteins. *J. Mol. Biol.* **76**, 241–256 (1973).
66. Medvedev, K. E., Kinch, L. N., Dustin Schaeffer, R., Pei, J. & Grishin, N. V. A fifth of the protein world: Rossmann-like proteins as an evolutionarily successful structural unit. *J. Mol. Biol.* **433**, 166788 (2021).
67. Sillitoe, I. et al. CATH: increased structural coverage of functional space. *Nucleic Acids Res.* **49**, D266–D273 (2021).
68. Bücher, T. & Klingenberg, M. Wege des Wasserstoffs in der lebendigen organisation. *Angew. Chem.* **70**, 552–570 (1958).
69. Agapakis, C. M. & Silver, P. A. Modular electron transfer circuits for synthetic biology. *Bioeng. Bugs* **1**, 413–418 (2010).
70. Rutter, J., Reick, M., Wu, L. C. & McKnight, S. L. Regulation of crock and NPAS2 DNA binding by the redox state of NAD cofactors. *Science* **293**, 510–514 (2001).
71. Atkinson, J. T. et al. Metalloprotein switches that display chemical-dependent electron transfer in cells. *Nat. Chem. Biol.* **15**, 189–195 (2019).
72. Huang, G. et al. Circadian oscillations of NADH redox state using a heterologous metabolic sensor in mammalian cells. *J. Biol. Chem.* **291**, 23906–23914 (2016).

Methods

Media and growth conditions

Culture for cloning was routinely performed with the *E. coli* XL-1 Blue strain and protein expression was generally carried out in the *E. coli* BL21(DE3) strain (Supplementary Table 1). Unless otherwise noted, all *E. coli* cultures were grown in 2× yeast extract tryptone (YT) medium prepared from ready-to-use medium granules at 31 g l^{-1} (Fisher Bioreagents 2× YT broth granulated medium: 16 g l^{-1} casein peptone, 10 g l^{-1} yeast extract and 5 g l^{-1} NaCl). When appropriate, selective medium was prepared at working concentrations of ampicillin (100 mg l^{-1}), spectinomycin (50 mg l^{-1}), kanamycin (50 mg l^{-1}) or chloramphenicol (20 mg l^{-1} from an ethanol-solvated stock). Generally, strains were cultured at 37 °C with 250 r.p.m. agitation on a 1-inch-diameter orbit and induction was initiated with final concentrations of 0.1% L-arabinose for strains containing the P_{BAD} promoter and 0.5 mM IPTG for strains containing the P_{LlacO1} promoter, unless otherwise noted. Buffer compositions are detailed in the Supplementary Methods. Commercially available key resources can be found in Supplementary Data.

Plasmid construction

Standard PCR reactions were performed using the PrimeSTAR Max DNA polymerase or KOD One PCR master mix -Blue-. Splicing by overlap extension PCR was performed with the KOD Xtreme hot start DNA polymerase. Generally, plasmids were constructed by PCR amplification of the target gene, with appropriate ~20–30-bp overlapping regions for downstream Gibson assembly[73] included in the primers. Constructs were circularized with a vector backbone by Gibson assembly and then introduced to XL-1 Blue mix and Go chemical competent cells, miniprepped and sequenced (Laragen) as previously described[12]. pDA063 was constructed by amplification of the *bdhA* gene from a *B. subtilis* ATCC 6051 genome template. Plasmids containing previously reported genes were subcloned from plasmids[74] (Supplementary Table 1).

Reported plasmid constructs from synthetic genes such as *L. lactis nox* were ordered from Integrated DNA Technologies (IDT) as gBlocks gene fragments with codon optimization performed by the IDT codon optimization webtool for *E. coli* K12. All bioprospected genes were prepared as synthetic DNA. DNA fragments were designed with the appropriate ~30-bp Gibson overlapping sequences on each end for direct circularization into vector backbones by Gibson assembly. Plasmids encoding mutants were built through site-directed mutagenesis as previously described[12] or encoded in the synthetic DNA design.

Site-saturated mutagenesis library construction

pYZ100 was constructed by performing standard PCR reactions described above using designed primers containing degenerate codon (NNK) at the target sites and a ~20–30-bp overlapping region for downstream Gibson assembly[73]. Circularized reaction products were desalted and concentrated with a DNA Clean and Concentrator kit. ElectroMAX DH10β competent cells were transformed by electroporation with the concentrated DNA product. Cells were rescued with SOC (super optimal with catabolic repressor) medium for 1 h at 37 °C with shaking and added to 20 ml of 2× YT medium with appropriate antibiotics for 10 h at 37 °C. Determination of the library size was performed as previously described[28]. Plasmid library DNA was isolated from the 20-ml culture by miniprep.

Strain construction

Strain MX102 R^0 was constructed by removal of the kanamycin resistance marker using the pCP20 plasmid (Supplementary Table 1) from the previously reported strain[12].

Protein expression and purification

Expression of recombinant protein was performed by introduction of the target plasmid into BL21(DE3) mix and Go chemical competent cells (Supplementary Table 1). A single colony was inoculated into 4 ml of 2× YT with 200 mg l^{-1} ampicillin and grown for ~14–16 h at 30 °C. Then, 2× YT with 200 mg l^{-1} ampicillin was inoculated to an optical density at 600 nm (OD_{600}) of 0.07 and incubated while shaking for approximately 1 h and 45 min at 37 °C. The cultures were removed from the shaker and placed at room temperature for 30 min without shaking, induced with 0.5 mM IPTG and then incubated while shaking at 30 °C for 24 h. Cells were harvested by centrifugation at 2,500*g* for 30 min at 4 °C. The supernatant was decanted and cell pellets were stored at −80 °C until purification. Cell lysis was performed mechanically and purification was performed following a modified version of the His-Protein Miniprep detailed in the Supplementary Methods. Protein quantification was achieved by Bradford assay. Purified protein was stored with 20% glycerol at −80 °C.

Preparation and purification of NMNH

NMNH was prepared enzymatically and purified as described previously[28].

Specific activity assay

Specific activity assays performed to characterize *Kp m*-Bdh homologs were performed in the following conditions: 50 mM Tris-Cl pH 8.0, (*R*/*S*)-Ac at 10 mM and 0.2 mM reduced cofactor at 30 °C. Then, 100-µl reactions were prepared by the addition of master mix to 10 µl of each enzyme. Enzyme was stored in His-Elution buffer with 20% glycerol (from a 50% glycerol stock). Initial reaction rates were determined from the slope of the first 60–100 s of reaction. Reaction rates were recorded as the difference between substrate and the no-substrate control. The production or consumption of reduced cofactor was detected with a SpectraMax M3 spectrophotometer at 340 nm, where the extinction coefficient used for the calculation was 6.22 mM^{-1} cm^{-1} for the NAD(P)H reaction rate or 4.89 mM^{-1} cm^{-1} for NMNH. One unit of enzymatic activity was defined as the quantity of enzyme required to produce or consume 1 µmol of reduced cofactor (NADH, NADPH or NMNH) per minute under the enzyme assay conditions described.

Specific activity assays performed to characterize the *Bs* (*R*)-Bdh homologs were carried out in the following conditions: 50 mM glycine–NaOH pH 10.0, 10 mM *m*-BDO and 4 mM oxidized cofactor. Specific activity assays of Nox variants were carried out in the following conditions: 50 mM Tris-Cl pH 7.0 with 0.3 mM reduced cofactor at 37 °C. The reaction rate was calculated as the difference between the no-cofactor control and the cofactor reaction to account for any potential nonspecific absorbance decrease at 340 nm in the absence of the addition of reduced cofactor. The dilution buffer for Nox was 50 mM Tris-Cl at pH 7.0. Unless otherwise noted, the handling of enzymes, initiation of reaction and calculation of reaction velocity were performed as described above.

Apparent kinetic parameter determination

Apparent Michaelis–Menten kinetic parameters for cofactors were determined by nonlinear fit of recorded initial reaction rate data to the Michaelis–Menten equation below, where v_0 is the initial rate, E_T is the total enzyme concentration and C is the varying cofactor concentration. For Bdhs, the kinetic parameters k_{cat} and K_m describe the apparent turnover number and apparent Michaelis constant at 50 mM substrate, respectively.

$$v_0 = \frac{E_T k_{cat} C}{K_m + C}$$

For *Ser* (*S*)-Bdh, the assay conditions were 30 °C, 50 mM Tris-Cl pH 8.0 and 50 mM (*SS*)-BDO, with the cofactor concentration varied. For *Kp m*-Bdh, the same assay conditions were used but with 50 mM *m*-BDO. For *Ll* Nox, the assay conditions were 37 °C and 50 mM Tris-Cl pH 7.0, with the reduced cofactor concentration varied.

Under conditions where the enzyme could not be saturated with cofactor ($K_m \gg C$), the initial rate data were instead recorded and fit to

a linear form of the Michaelis–Menten equation to solve for catalytic efficiency, k_{cat}/K_m.

$$v_0 = \frac{E_T k_{cat} C}{K_m}$$

Gas chromatography

All gas chromatography (GC) was performed with an Agilent 6850 (Agilent Technologies) coupled to a flame ionization detector with data collected with ChemStation B.04.03. All gases were purchased from Airgas. The Agilent CP ChiraSilDex CB (25 m × 0.25-mm inner diameter × 0.25-µm film thickness × 5-inch cage) was used for all separations. A method was developed with the following parameters: The inlet was heated to 250 °C with a pressure of 25.0 psi. The injection volume was 1 µl. The inlet was set to split at a ratio of 20:1 with helium used as the carrier gas. The GC was operated in constant-pressure mode at 25.0 psi. The oven program started at 80 °C, was held for 10 min and then was increased at 10 °C per min to 110 °C, followed by a 20 °C per min increase to 200 °C with a 2-min hold. The flame ionization detector was set to 275 °C, 40 mL min^{-1} H_2 and 350 mL min^{-1} air, with a makeup helium flow of 45 ml min^{-1}. The elution order observed was (*R*)-Ac, (*S*)-Ac, (*SS*)-BDO, (*RR*)-BDO, *m*-BDO and then internal standard, 4-oxoisophorone. Samples for GC analysis were processed by a salting-out-extraction with ethyl acetate, as detailed in the Supplementary Methods. The determination of retention times is also provided in the Supplementary Methods.

Purified protein cycling reactions

Cycling reactions consisting of purified proteins were prepared similarly to previous research[12]. Reactions were initiated by addition of a mixture of each reaction's enzymes to a master mix containing all other components. For determination of enzyme stereospecificity, reaction mixtures contained 100 mM potassium phosphate pH 7.5, 1 M NaCl, 200 mM D-glucose, 2 mM oxidized cofactor and 5 g l^{-1} racemic Ac. The final concentration of enzyme in the reaction was 11.7 µM GDH Ortho and 28.1 µM Bdh. All molar protein concentrations are reported on the basis of the molecular weight of the monomers. Then, 350-µl reactions were incubated in 15-ml conical tubes at a 45° angle, 30 °C, 250 r.p.m. for 4 h before GC analysis as described above. Analogous reactions for (*R*)-Bdh bioprospecting are described in the Supplementary Methods.

For the single-cofactor model systems, 5 g l^{-1} *m*-BDO, 2 mM NAD^+, 100 mM potassium phosphate, 200 mM MOPS pH 8.0, 10 µM *Ser* (*S*)-Bdh WT and 5 µM *Bs* (*R*)-Bdh were provided. Cofactor-recycling enzymes consisted of 10 µM *Lb* Nox or 10 µM GDH WT as appropriate. Then, 450-µl reactions were incubated while shaking for 48 h at 30 °C before sample analysis by GC.

For the *m*-BDO-to-(*SS*)-BDO reaction cascade using NAD^+ and NMN^+ (Figs. 1a and 4a), the 900-µl reaction contained 300 mM Tris-Cl pH 8.0, 1 M NaCl, 200 mM D-glucose, 2 mM oxidized cofactor and 5 g l^{-1} *m*-BDO. The protein ratio used was 10 µM *Lb* Nox, 5 µM *Bs* (*R*)-Bdh, 20 µM GDH Ortho and 60 µM *Ser* (*S*)-Bdh Ortho. For the $NADP^+$ and NMN^+ system (Figs. 1c and 4g), the protein ratio used was 20 µM Tp Nox, 10 µM *Cs* (*R*)-Bdh, 20 µM GDH Ortho and 60 µM *Ser* (*S*)-Bdh Ortho and the reaction volume was 700 µl. Reactions to produce (*SS*)-BDO were sampled after 24 h or 72 h at 30 °C for GC analysis.

For the *m*-BDO-to-(*RR*)-BDO reaction cascade using NAD^+ and NMN^+, the 700-µl reactions contained 300 mM Tris-Cl pH 8.0, 1 M NaCl, 200 mM D-glucose, 2 mM NMN^+, 0.2 mM NAD^+ and 2 g l^{-1} *m*-BDO. Because the determination of K_m for Nox Ortho with NAD(P)H was technically limited, a specific activity assay of Nox Ortho with each cofactor was prototyped to guide system design (Supplementary Fig. 11). The concentration of $NAD(P)^+$ in these systems was 0.2 mM. The protein ratio was 10 µM Nox Ortho, 60 µM *Kp* (*S*)-Bdh Ortho, 5 µM *Bs* GDH and 5 µM *Bs* (*R*)-Bdh. For the $NADP^+$ and NMN^+ system, $NADP^+$ was substituted for NAD^+ and 5 µM *Cs* (*R*)-Bdh was substituted for *Bs* (*R*)-Bdh. Reactions to produce (*RR*)-BDO were sampled after 72 h at 30 °C for GC analysis.

Standard selection protocol of *Ll* Nox libraries and control plasmids used in MX502

The strain construction and standard selection were performed as described previously[28]. Plasmids pLS501 (XenA D116E) and pYZ10 (*Ll* Nox WT) served as positive and negative controls, respectively. Plasmid pYZ20 (*Ll* Nox I159T) was also transformed as a library template control as a benchmark.

Selection of *Ll* Nox library pYZ100

The library culture was obtained by following the standard selection protocol described above, and was washed three times in M9 wash buffer and diluted to a final concentration of ~10^5 cells per ml in M9 wash buffer. Then, 40 µl of this suspension was plated on each of seven M9 selection plates with 20 g l^{-1} D-glucose and 2 mM NMN^+. Plates were incubated at 30 °C and monitored periodically for 10 days. After 10 days, six colonies from each plate and colonies from the control plates were streaked onto fresh M9 selection plates to isolate variants and validate growth. After 7 days, plates were evaluated for growth and 18 colonies with diverse growth phenotypes were selected for sequencing (Supplementary Table 2) and NMNH activity characterization. Colonies were cultured in 2× YT liquid medium overnight and plasmids were extracted using a QIAprep Spin Miniprep kit.

Reformulation of commercial redox ratio kits for NMNH:NMN^+ quantification

The Amplite colorimetric NADH assay kit (AAT Bioquest), with some components from the redox ratio kits, was reformulated to prepare an NMNH:NMN^+ kit. The NAD^+:NADH ratio and $NADP^+$:NADPH ratio quantification was performed according to the kit's instructions with additional preassay sample-processing steps to remove enzymes, as detailed in the Supplementary Methods. The NMNH:NMN^+ reformulated kit method is detailed in the Supplementary Methods. Briefly, the difference between the NADH assay kit and the redox ratio kits is the addition of a selective reduced cofactor degradation step and cofactor-specific enzymatic recycling. Therefore, we prepared the NMNH:NMN^+ ratio quantification kit by using the selective cofactor degradation solutions from the redox ratio kits with the addition of a strictly NMN^+-specific reducing enzyme, GDH Ortho[12], to the final colorimetric assay master mix solution. Data for Fig. 4c,f,i,l corresponding to systems in Fig. 1a–d were sampled at 48 h, 72 h, 48 h and 24 h, respectively.

Resting cell biotransformation

All necessary plasmids were inserted into strain MX102 R^0 by electroporation and plated on 2× YT with 200 mg l^{-1} ampicillin, 50 mg l^{-1} spectinomycin and 50 mg l^{-1} kanamycin (YT-ASK). Triplicate seed cultures of 4 ml of 2× YT-ASK with 5 g l^{-1} D-mannitol were prepared from single colonies and grown at 37 °C for 16 h. Cell cultivation cultures were normalized to an OD_{600} of 0.04 in 50 ml of 2× YT-ASK with 10 g l^{-1} D-mannitol and 0.5 mM 5-aminolevunic acid. The cells were incubated while shaking for 4 h at 30 °C and then induced with 0.5 mM IPTG and 0.1% (w/v) L-arabinose. After induction, cells were incubated for 12 h while shaking at 30 °C before harvest. At harvest, the OD_{600} of each culture was determined and the volume of cells necessary to prepare a final suspension with an OD_{600} of 100 in a 3-ml final volume was transferred to 50-ml conical tubes and pelleted at 2,500*g* for 10 min at room temperature. The pelleted cells were washed by gentle resuspension and centrifugation twice in 40 ml of 100 mM potassium phosphate pH 7.5 at room temperature, then washed one more time in 10 ml of the same and transferred to 15-ml conical tubes. The conical tubes were pelleted a final time and resuspended to a total volume of 3 ml.

The resting cell reactions were initiated by the addition of 600 µl of washed cell suspension to 2.4 ml of concentrated reaction master mix in 15-ml conical tubes. The reaction mixture was composed of 200 mM D-glucose, 0 or 10 mM NMN^+, 5 g l^{-1} *m*-BDO, 0.5 mM IPTG, 100 mM dibasic potassium phosphate, 200 mM MOPS, ASK and 0.1% (w/v) L-arabinose. Resting cell reactions were then incubated horizontally at 250 r.p.m. for 48 h at 30 °C. Resting cell reactions with Tp Nox expressed were instead incubated at 18 °C for 152 h.

Rosetta molecular simulations

The *Ll* Nox, *Kp m*-Bdh and *Ser* (*S*)-Bdh structures were generated by AlphaFold[75] and subsequently relaxed using a backbone-constrained FastRelax procedure[76]. The NMN^+, NAD^+ and $NADP^+$ conformer library used was previously established[30]. Initial coordinates for NMN^+ were obtained by aligning the *Ll* Nox structure to the homologous structure PDB 2BC0 (ref. 77). Initial coordinates for NMN^+ in *Kp m*-Bdh and *Ser* (*S*)-Bdh were obtained by alignment to the homologous structures PDB 1GEG (ref. 56) and PDB 3A28 (ref. 78), respectively.

A detailed method for *Ll* Nox is given below. Bdhs were simulated in the same manner with the exclusion of flavin adenine dinucleotide (FAD^+). For each simulation, one of the cofactors and FAD^+ were placed into the active site and the enzyme–ligand complex was optimized. The EnzRepackMinimize protocol was applied to predict the WT structure bound with NMN^+ and amino acid substitutions that improve binding affinity for NMN^+ (ref. 79). This process involved Monte Carlo evaluation, sampling alternative rotamers, side-chain substitutions and backbone minimization to examine different binding-pocket geometries. Restraints were imposed to maintain the cofactors in a catalytically competent geometry for hydride transfer and interactions with FAD^+. After 2,000 simulations for each batch, the top 20 outputs based on constraint score, protein–ligand interface energy score and total system energy score were visually examined. For ligand docking simulations with substitutions, the corresponding substitutions were generated using the MutateResidue mover in RosettaScripts[79]. Example run files, constraints, options, RosettaScripts XML files and ligand param files are available on Zenodo (https://doi.org/10.5281/zenodo.11478967)[80].

MD simulations

The docking structures were picked as initial structures for subsequent MD simulations. The CHARMM36m force field with cross term map correction[81] and CHARMM general force field[82] were selected for parameterizing proteins and cofactors, such as FAD and NMNH, respectively. For both WT and mutants (LLNox_LL9), structures were all centered in a periodic cubic box of 72 × 82 × 90 Å and solvated using the TIP3P water model[83]. Sodium and chloride ions were added for neutralization and the ionic concentration was maintained at 150 mM. Both systems were equilibrated using the NVT ensemble over 200 ps with Cα atoms of protein and heteroatoms of FAD and NMNH fixed. A 10-ns NPT simulation was performed with the same atomic constraints while decreasing from 100 to 0 kcal per mol per $Å^2$ gradually at the interval of 2 ns. Lastly, a 100-ns NPT simulation was collected without constraints. Throughout, temperature and pressure were held at 310 K and 1 atm using Langevin dynamics and Nose–Hoover–Langevin piston (excluding hydrogen atoms), respectively[84]. Particle mesh Ewald summation[85] with a 12-Å cutoff was used for electrostatic calculations. The integration time step was set to 2 fs using the SHAKE algorithm[86]. All MD simulations were conducted using package suite NAMD 2.14 (ref. 87). For hydrogen-bond analysis, the threshold distance between donor and acceptor and the donor–hydrogen–acceptor angle were 3 Å and 20°, respectively. Analysis was conducted over the phosphate group of NMNH and protein with VMD[88]. Only the last 60 ns of the trajectory was used. The input, topology and parameter files are available on Zenodo (https://doi.org/10.5281/zenodo.11478967)[80].

Structural alignment of the Rossmann family

The structural alignment within the CATH superfamily 3.40.50.720 was performed with the >35 % sequence identity domain cluster representatives as calculated in the CATH database[67]. At the time of this publication, the PyMOL session of the superfamily superposition was not available for download; thus, crystal structures and their specified chains listed in Table S5 of Toledo-Patiño et al.'s work[64] were aggregated into a single PyMOL session. Structures with an NAD ligand were aligned with the PyMOL alignment tool according to their atomic coordinates. The pairwise root-mean-square deviation (r.m.s.d.) for all pairs was calculated using TM-align[89]. On the basis of the pairwise r.m.s.d., the crystal structures were clustered using the SciPy python library[90] and organized into eight groups with a cutoff distance of 33 on the resultant dendrogram. These eight groups were aligned using the PyMOL alignment tool to a structure with an NAD ligand from each group as the reference structure for that cluster. For visualization of the structural conservation, the backbones of the structures in the alignment are shown as transparent cartoon loops.

Reporting summary

Further information on research design is available in the Nature Portfolio Reporting Summary linked to this article.

Data availability

Information on the strains and plasmids used in this study is available in Supplementary Data. Accession codes for genes investigated in this study can be found in Supplementary Tables 4 and 5. All DNA sequence and structural information used is publicly available (*Ser* Bdh2, UniProt A0A7U3Z3T2; *Kp* Dar, UniProt D7RP28; *Bs* BdhA, UniProt O34788; *Cs* Bdh, UniProt M1MWX5; *Bs* Gdh, UniProt P12310; *Ll* Nox, UniProt A2RIB7; *Lb* Nox, UniProt Q03Q85, PDB 5VN0; Tp Nox (*Lb* Nox G159A;D177A;A178R;M179S;P184R); *Ecl* Dar, GenBank JN035909; *Kp* BudC, PDB 1GEG; *Ka* BudC, National Center for Biotechnology Information (NCBI) Ref WP_015366942; *Ka* Dar, GenBank VEC79507; *Ko* BudC, GenBank AEX06195; *As* Bdh, GenBank NLH91458; *Cr* Bdh, GenBank AEI90716; *Ca* Bdh, NCBI Ref WP_073006451; *Pb* Bdh, NCBI Ref WP_148550966; *Cbo* Bdh, NCBI Ref WP_075141790; *Km* Bdh, NCBI Ref WP_102401827; *Cbu* Bdh, NCBI Ref WP_104675707; *Zp* Bdh, NCBI Ref WP_027704711). All data generated in this study are provided in the Supplementary Information. Source data are provided with this paper.

Code availability

The input files and source code for the Rosetta molecular simulation and MD simulations are publicly accessible on Zenodo (https://doi.org/10.5281/zenodo.11478967)[80].

References

73. Gibson, D. G. et al. Enzymatic assembly of DNA molecules up to several hundred kilobases. *Nat. Methods* **6**, 343–345 (2009).
74. Maxel, S. et al. A growth-based, high-throughput selection platform enables remodeling of 4-hydroxybenzoate hydroxylase active site. *ACS Catal.* **10**, 6969–6974 (2020).
75. Jumper, J. et al. Highly accurate protein structure prediction with AlphaFold. *Nature* **596**, 583–589 (2021).
76. Tyka, M. D. et al. Alternate states of proteins revealed by detailed energy landscape mapping. *J. Mol. Biol.* **405**, 607–618 (2011).
77. Wallen, J. R. et al. Structural analysis of *Streptococcus pyogenes* NADH oxidase: conformational dynamics involved in formation of the C(4a)-peroxyflavin intermediate. *Biochemistry* **54**, 6815–6829 (2015).
78. Otagiri, M. et al. Structural basis for chiral substrate recognition by two 2,3-butanediol dehydrogenases. *FEBS Lett.* **584**, 219–223 (2010).

79. Fleishman, S. J. et al. RosettaScripts: a scripting language interface to the Rosetta macromolecular modeling suite. *PLoS ONE* **6**, e20161 (2011).
80. Zhu, Q. Rosetta files related to the engineering of Nox and Bdh enzymes. *Zenodo* https://doi.org/10.5281/zenodo.11478967 (2024).
81. Huang, J. et al. CHARMM36m: an improved force field for folded and intrinsically disordered proteins. *Nat. Methods* **14**, 71–73 (2017).
82. Vanommeslaeghe, K. et al. CHARMM general force field: a force field for drug-like molecules compatible with the CHARMM all-atom additive biological force fields. *J. Comput. Chem.* **31**, 671–690 (2010).
83. Jorgensen, W. L., Chandrasekhar, J., Madura, J. D., Impey, R. W. & Klein, M. L. Comparison of simple potential functions for simulating liquid water. *J. Chem. Phys.* **79**, 926–935 (1983).
84. Feller, S. E., Zhang, Y., Pastor, R. W. & Brooks, B. R. Constant pressure molecular dynamics simulation: the Langevin piston method. *J. Chem. Phys.* **103**, 4613–4621 (1995).
85. Darden, T., York, D. & Pedersen, L. Particle mesh Ewald: An *N*·log(*N*) method for Ewald sums in large systems. *J. Chem. Phys.* **98**, 10089–10092 (1993).
86. Allen, M. P. & Tildesley, D. J. *Computer Simulation of Liquids* 2nd edn (Oxford University Press, 2017).
87. Phillips, J. C. et al. Scalable molecular dynamics on CPU and GPU architectures with NAMD. *J. Chem. Phys.* **153**, 044130 (2020).
88. Humphrey, W., Dalke, A. & Schulten, K. VMD: visual molecular dynamics. *J. Mol. Graph.* **14**, 33–38 (1996).
89. Zhang, Y. TM-align: a protein structure alignment algorithm based on the TM-score. *Nucleic Acids Res.* **33**, 2302–2309 (2005).
90. Virtanen, P. et al. SciPy 1.0: fundamental algorithms for scientific computing in Python. *Nat. Methods* **17**, 261–272 (2020).

Acknowledgements

H.L. acknowledges support from the University of California, Irvine, the National Science Foundation (NSF) (award nos. 1847705 and MCB-2328145), the National Institutes of Health (NIH) (award no. DP2 GM137427), an Alfred Sloan research fellowship and the Advanced Research Projects Agency—Energy (award no. DE-AR0001508). Y.C., E.L. and J.B.S. acknowledge the funding of the National Institute of Environmental Health Sciences (grant no. P42ES004699), the NIH (grant no. R01 GM 076324-11) and the NSF (grant nos. 1627539, 1805510 and 1827246). R.L. acknowledges support from the NIH (award no. R35 GM130367). D.A acknowledges support from the NSF Graduate Research Fellowship Program (grant no. DGE1839285). We acknowledge valuable technical support provided by AAT Bioquest for the redox ratio kits.

Author contributions

D.A., Y.Z., E.K. and H.L. designed the experiments. Y.C. and E.L. performed Rosetta modeling. E.L. and D.A. performed bioinformatic analysis of the NAD(P)-binding Rossmann-like domain superfamily. E.K. and Y.Z. performed rational protein engineering experiments. Y.Z. performed growth-based selection of Nox. Q.Z., Y.W. and R.L. performed MD simulations and analyzed the results. D.A. and E.K. bioprospected Bdh homologs. D.A. performed the Michaelis–Menten kinetic experiments for Bdhs. Y.Z. performed the Michaelis–Menten kinetic experiments for Nox. D.A. and S.P. performed cell-free biotransformation experiments. D.A. performed the resting cell biotransformation experiments. W.B.B. and D.A. reformulated the colorimetric redox ratio assay. D.A. performed the colorimetric redox ratio assays. Y.C., E.L. and J.B.S. analyzed the modeling results. All authors analyzed the data and wrote the paper.

Competing interests

The authors declare no competing interests.

Additional information

Supplementary information The online version contains supplementary material available at https://doi.org/10.1038/s41589-024-01702-5.

Correspondence and requests for materials should be addressed to Han Li.

Peer review information *Nature Chemical Biology* thanks Zhen Chen, Steffen Lindner and Carine Vergne-Vaxelaire for their contribution to the peer review of this work.

nature portfolio

Corresponding author(s): Han Li

Last updated by author(s): June 30, 2024

Reporting Summary

Nature Portfolio wishes to improve the reproducibility of the work that we publish. This form provides structure for consistency and transparency in reporting. For further information on Nature Portfolio policies, see our Editorial Policies and the Editorial Policy Checklist.

Statistics

For all statistical analyses, confirm that the following items are present in the figure legend, table legend, main text, or Methods section.

n/a	Confirmed
☐	☒ The exact sample size (*n*) for each experimental group/condition, given as a discrete number and unit of measurement
☐	☒ A statement on whether measurements were taken from distinct samples or whether the same sample was measured repeatedly
☐	☒ The statistical test(s) used AND whether they are one- or two-sided *Only common tests should be described solely by name; describe more complex techniques in the Methods section.*
☒	☐ A description of all covariates tested
☐	☒ A description of any assumptions or corrections, such as tests of normality and adjustment for multiple comparisons
☐	☒ A full description of the statistical parameters including central tendency (e.g. means) or other basic estimates (e.g. regression coefficient) AND variation (e.g. standard deviation) or associated estimates of uncertainty (e.g. confidence intervals)
☐	☒ For null hypothesis testing, the test statistic (e.g. *F*, *t*, *r*) with confidence intervals, effect sizes, degrees of freedom and *P* value noted *Give P values as exact values whenever suitable.*
☒	☐ For Bayesian analysis, information on the choice of priors and Markov chain Monte Carlo settings
☒	☐ For hierarchical and complex designs, identification of the appropriate level for tests and full reporting of outcomes
☒	☐ Estimates of effect sizes (e.g. Cohen's *d*, Pearson's *r*), indicating how they were calculated

Our web collection on statistics for biologists contains articles on many of the points above.

Software and code

Policy information about availability of computer code

Data collection	The structures for Ll Nox, Kp m-Bdh, and Ser S-Bdh were generated with Alphafold v2.0.0. Mutant structures and Rosetta molecular simulations were created with Rosetta version 2018.24.post.dev+17.master.450949e 450949e481542459ae6534e867a61fe9709846be. The enzymatic assay data were collected with SpectraMax M3 microplate reader. GC data were collected using ChemStation B.04.03. The Rossmann family structural clustering was performed with TM-align 20150914 and python 3.10.12 and the packages: numpy 1.25.2, pandas 2.0.3, scipy 1.11.4, and matplotlib 3.7.1. The Rossmann family alignment and visualization was generated with PyMOL version 2.5.4. Molecular dynamics simulations were conducted using NAMD 2.14 with all bonds involving hydrogen held rigid using SHAKE algorithm.
Data analysis	Hydrogen bond analysis derived from molecular dynamics simulations was conducted with the help of VMD 1.9.4a57 for Linux. Other data analysis were performed using Microsoft Excel 16 for Windows and Microsoft Excel 16.83 for Mac.

For manuscripts utilizing custom algorithms or software that are central to the research but not yet described in published literature, software must be made available to editors and reviewers. We strongly encourage code deposition in a community repository (e.g. GitHub). See the Nature Portfolio guidelines for submitting code & software for further information.

Data

Policy information about availability of data

All manuscripts must include a data availability statement. This statement should provide the following information, where applicable:

- Accession codes, unique identifiers, or web links for publicly available datasets
- A description of any restrictions on data availability
- For clinical datasets or third party data, please ensure that the statement adheres to our policy

All data that support the findings of the study are available within the main text, the supplementary information, and source data file. All DNA sequence and structural information used are publicly available (Ser Bdh2, uniprot: A0A7U3Z3T2; Kp Dar, uniprot: D7RP28; Bs BdhA, uniprot: O34788; Cs Bdh, uniprot: M1MWX5; Bs Gdh, uniprot: P12310; Ll Nox, uniprot: A2RIB7; Lb Nox, uniprot: Q03Q85, PDB: 5VN0; Tp Nox (Lb Nox G159A-D177A-A178R-M179S-P184R); Ecl Dar, GenBank: JN035909; Kp BudC, PDB: 1GEG; Ka BudC, NCBI Ref: WP_015366942; Ka Dar, GenBank: VEC79507; Ko BudC, GenBank: AEX06195; As Bdh, GenBank: NLH91458; Cr Bdh, GenBank: AEI90716; Ca Bdh, NCBI Ref: WP_073006451; Pb Bdh, NCBI Ref: WP_148550966; Cbo Bdh, NCBI Ref: WP_075141790; Km Bdh, NCBI Ref: WP_102401827; Cbu Bdh, NCBI Ref: WP_104675707; Zp Bdh, NCBI Ref: WP_027704711). Raw data for Figures 1, 2, 3, 4, 5 and 6 are provided in the source data file. The source codes for Rosetta Molecular simulation and molecular dynamic simulations are publicly accessible on Zenodo [https://doi.org/10.5281/zenodo.11478967].

Human research participants

Policy information about studies involving human research participants and Sex and Gender in Research.

Reporting on sex and gender	There is no human research participants in this study.
Population characteristics	There is no human research participants in this study.
Recruitment	There is no human research participants in this study.
Ethics oversight	There is no human research participants in this study.

Note that full information on the approval of the study protocol must also be provided in the manuscript.

Field-specific reporting

Please select the one below that is the best fit for your research. If you are not sure, read the appropriate sections before making your selection.

☒ Life sciences ☐ Behavioural & social sciences ☐ Ecological, evolutionary & environmental sciences

For a reference copy of the document with all sections, see nature.com/documents/nr-reporting-summary-flat.pdf

Life sciences study design

All studies must disclose on these points even when the disclosure is negative.

Sample size	All experiments were performed in at least triplicate (n=3), except for data generated during the initial bioprospecting screening or assay development process, which are in duplicates (n=2). The sample size was chosen according to community standards.
Data exclusions	No data were excluded from analyses.
Replication	All replication attempts were successful. Every time experiments were conducted, controls with known values were included alongside the unknown samples, and the control values were consistent with those from previous trials
Randomization	All cultures and samples in the same experiment were treated identically. Therefore, randomization was not relevant.
Blinding	This study reports objective measurements of samples derived from bacterial culture, purified proteins, or chemical reactions. In each experiment, the samples were treated identically. Therefore, blinding was not relevent.

Reporting for specific materials, systems and methods

We require information from authors about some types of materials, experimental systems and methods used in many studies. Here, indicate whether each material, system or method listed is relevant to your study. If you are not sure if a list item applies to your research, read the appropriate section before selecting a response.

Materials & experimental systems

n/a	Involved in the study
☒	☐ Antibodies
☒	☐ Eukaryotic cell lines
☒	☐ Palaeontology and archaeology
☒	☐ Animals and other organisms
☒	☐ Clinical data
☒	☐ Dual use research of concern

Methods

n/a	Involved in the study
☒	☐ ChIP-seq
☒	☐ Flow cytometry
☒	☐ MRI-based neuroimaging